Department of Precision and Microsystems Engineering

Topology optimization of compliant mechanisms
With focus on overheating prevention during Additive Manufacturing

J.O.Y. Huisman

Report no	: 2021.033
Coach	: Rajit Ranjan
Professor	: Matthijs Langelaar
Specialisation	: SOM
Type of report	: Master Thesis
Date	: 21 June 2021

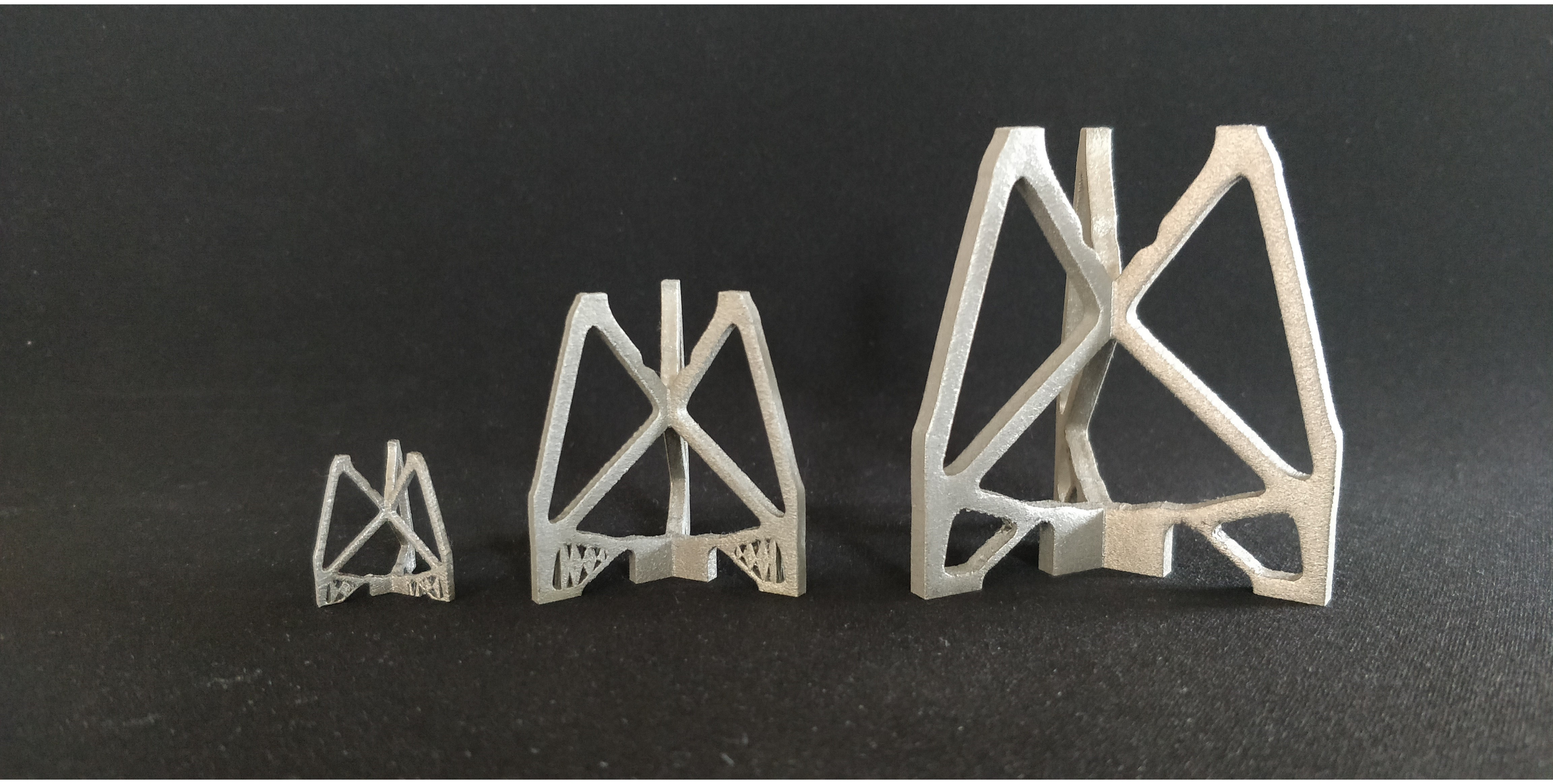

Delft University of Technology

Precision and Microsystems Engineering

Challenge the future

Topology optimization of compliant mechanisms

With focus on overheating prevention during Additive Manufacturing

by

J.O.Y. Huisman

to obtain the degree of Master of Science
at the Delft University of Technology,
to be defended on Monday June 21, 2021 at 3:00 PM.

Abstract

A compliant mechanism (CM) is a special kind of mechanism which has seen an increase in use in various high-tech applications. A CM is a structure designed with the intention to deform: motion is achieved by deformation of flexible members of its body. CMs are designed by topology optimization (TO) algorithms, which use boundary conditions as an input and give a design as an output. Additive manufacturing (AM) is used to fabricate the designed CMs, as geometric complexity is much less of a problem compared to conventional methods. One issue with AM is that local overheating during printing can cause defects in the design, specifically for metal designs, as the temperature is very high during printing. In this thesis, a CM is designed using TO and fabricated using AM. The design is then printed and analysed for overheating defects to determine if any defects due to overheating are present. Also, a computationally inexpensive AM model is integrated into the TO for CM, which can detect zones prone to local overheating. Next to that, the robust optimization method is used to obtain a design which needs much less post-processing. The obtained designs are compared to existing TO methods and it is found that the added constraint can reduce overheating by a large amount while maintaining a relatively high CM performance.

Preface

This thesis is the final result of my Master of Science graduation project at the department of Precision and Microsystems Engineering at the Technical University of Delft.

During the time working on this thesis, I have been helped by multiple people and I would like to thank them. First of all, I would like to thank Rajit Ranjan and Matthijs langelaar. They supervised and helped me, but also challenged me when needed. I would also like to thank Mary Frecker from the Pennsylvania State University for her support during my time at Penn State and for the opportunity to print my own metal compliant mechanism.

Lastly I would like to thank Manon, my family and my friends for their support.

J.O.Y. Huisman
Wognum, June 2021

Contents

1

Introduction

This chapter introduces the topics of this thesis, states the problem, explains the approach of this thesis and gives an overview of the chapters.

1.1. Background

Mechanisms have been around for a long time and have been constantly improved. In the last few decades, a special kind of mechanism has been utilized in various high-tech applications, namely compliant mechanisms (CMs). A CM is a structure designed with the intention to deform: motion is achieved by deformation of flexible members of its body. CMs are favoured above rigid mechanisms because they are usually created out of one piece of material and therefore have no friction, thus less wear, noise and backlash [15]. Although CMs enhance the functional performance, there are still certain challenges associated with designing and manufacturing them. Firstly, designing a CM can be very difficult, if done manually. Due to this, computer algorithms are often used to design a CM. The second challenge faced, is the fabrication of a CM. It is difficult to fabricate a three-dimensional CM using traditional manufacturing methods, since such CMs often have complex geometries. Specialized techniques, in particular 3D printing, show promising results for fabrication of complex CMs. Both the design and manufacturing of CMs are the subject of this thesis.

Figure 1.1: Metal compliant mechanism made by additive manufacturing [11]

A method which is widely used to design CMs is topology optimization (TO). It is a method which finds the optimal distribution of material in a pre-defined design domain for specified constraints [2]. The method optimizes a well-defined objective by iterative design changes. Different objectives can be used, for example: maximizing the output displacement, maximizing the geometric advantage or maximizing the stiffness of a design.

Additive manufacturing (AM), also known as 3D printing, is an increasingly popular method of manufacturing which uses powder or wire to produce a part in a layer-by-layer process from 3D model data [9]. Multiple materials can be used, ranging from plastics to metals. Designs acquired from TO can be more easily manufactured using AM than conventional methods because geometric complexity is much less of a problem due to the layer-by-layer approach. Metal 3D printing is increasingly being used as mainstream manufacturing method [9].

Powder bed fusion (PBF) consists of all processes where focused energy (laser or electron beam) is used to sinter or melt a certain part of a layer of a powder bed. In laser PBF, the most common technique used for printing metal parts, a laser is used to melt a selected part of a layer of powder. Subsequently, a new layer of powder is spread across and a selected part of the new layer is melted [19]. A new layer of material is typically 20–50 μm thick and the minimum feature size is 75–100 μm [26]. During the printing process, the heat flows from the topmost layer to the build platform. An illustration of such a PBF system can be seen in Fig. 1.2.

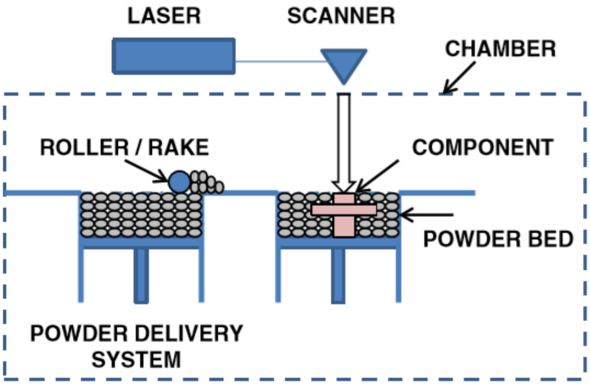

Figure 1.2: Illustration of a laser powder bed fusion system [9]

Although using AM to produce a CM has many advantages, there are also challenges. Designs which have been created using TO can have an organic-like structure, with thin members and large overhanging surfaces. This can be a problem because thin members are not able to adequately conduct heat applied by the laser. Furthermore, loose powder has a much lower conductivity compared to bulk material [8][14]. This results in heat accumulation and overheating near the melt zone, which results in defects, such as swelling, part distortion, melt balling or dross [14][16] and in the end, failure of the design. This is especially a problem for CMs, as they require a high part quality to obtain a desired motion. A solution to this, is to use AM constraints in the TO. Significant research has been done on manufacturability oriented TO [13]. Most research is done on support slimming or elimination, some research has been done on heat accumulation, however, the introduced methods have a large computational cost. Ranjan et al. [17] have introduced a low-cost method which uses a temperature constraint to prevent overheating in the design. This method has been tested for TO of stiff structures with promising results. In this thesis, the method will be investigated for CM designs.

1.2. Problem statement

As indicated by the previous section, during laser PBF of complex geometries, several problems arise. One of the main problems is overheating of the material during printing. The aims of this thesis are twofold:

1. To determine the extent of overheating defects in metal printed CMs generated by conventional TO
2. To determine the effectiveness of reducing overheating in TO-generated CMs by adding an overheating constraint in the TO process

1.3. Approach

To study the problems which may result from overheating during metal AM, a reference case was designed using TO without any form of overheating constraint. The reference case was examined to confirm the working principle of the design and to observe any overheating defects. The design and printing were done at Penn State University, in the EDOG lab of Prof. Mary Frecker. The examination was done at the TU Delft lab.

To answer the second research question, CMs were designed by TO with the temperature constraint introduced by Ranjan et al. [17]. In this process, also a new way to obtain clear and manufacturable designs was used. The plan was to also print the designs generated using overheating constrained TO, however due to the corona virus, this was not an option. Instead, the designs were evaluated using simulations. In the end, designs obtained with and without overheating constraint were compared to study the changes caused by the hotspot constraint.

1.4. Report structure

This thesis is divided into six chapters. Chapter 2 gives an overview on the state of the art regarding TO, CMs and temperature constraints. Chapter 3 introduces the reference case and evaluates the design. In Chapter 4, the experiment on the reference case is shown, as well as multiple simulations to analyse the reference case. Chapter 5 introduces the CMs hotspot TO and shows the different results obtained with different parameters. Also, a novel extension is introduced by combining the hotspot constraint with the robust formulation, which is found to improve the quality of the TO results. Finally, conclusions and recommendations are given in Chapter 6.

2

State of the art

This chapter provides a summary of the state of the art of topology optimization (TO) for compliant mechanisms and the hotspot constraint used in this thesis.

2.1. Topology optimization

Topology optimization (TO) is a method which seeks to find the optimal distribution of material for a given set of loads and supports. One of the first methods used in literature is the homogenization method, which was introduced by Bendsøe and Kikuchi [3]. This concept has been developed into several different approaches, from which the level set and density-based approaches are most common. The level set approach treats the problem as a shape optimization in which iterative boundary movements are used to optimize a part geometry. The density-based approach starts with discretising the design domain into a set of finite elements and then defining the material distribution by assigning material or voids to all the elements as can be seen in Fig. 2.1, where a black element represents material and a white element represents a void.

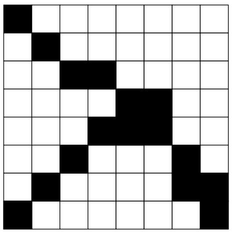

Figure 2.1: Grid representation of the density-based approach with both void and material elements

The level set approach has a clearly defined geometry throughout the optimization process and thus allows for explicitly formulating constraints, objectives and boundary conditions on the interface. The downside of the approach is an inability to generate new holes, which can be avoided by introducing a new step in the optimization process, but this method will affect the convergence of the entire optimization process [22]. The benefit of using a density-based approach is that it can be efficiently solved by well-established optimization algorithms such as the Optimality Criteria (OC) or the Method of Moving Asymptotes (MMA) [24]. The density-based approach also allows for systematic and straightforward inclusion of global constraints. This thesis focuses on the density-based approach because of these advantages, and because this method was used to create the hotspot constraint and therefore will give less complications during the implementation.

As mentioned, the design domain is discretized into a number of elements. These elements have a density of either zero or one, this is a discrete optimization problem which means the design derivatives cannot be computed. An example of such a design derivative is the derivative of the stiffness with respect to the density field. To solve the problem of having a discrete optimization problem, the element densities are relaxed and can take an intermediate value between zero and one. This converts the problem into a continuous optimization problem. The problem is then solved in an iterative manner, where the design derivatives are used to update the design until the objective converges to a stable minimum or maximum. The introduction of intermediate densities solves the problem of having a discrete optimization problem, it does however introduce a new problem: intermediate densities in the final solution which may be difficult to realise physically. Bendsøe and Sigmund [4] introduced a method which drives the solution towards a one/zero solution. This is done by putting a penalty on intermediate densities, through a method called Solid Isotropic Material with Penalization (SIMP). A minimum compliance optimization problem using SIMP can be written as

$$\min_{\rho} \quad c(\boldsymbol{\rho}) = \mathbf{U}^T\mathbf{K}\mathbf{U} = \sum_{e=1}^{N} (\rho_e)^p \mathbf{u}_e^T \mathbf{k}_0 \mathbf{u}_e, \tag{2.1a}$$

$$\text{Subject to} \quad \mathbf{K}\mathbf{U} = \mathbf{F}, \tag{2.1b}$$

$$\frac{V(\boldsymbol{\rho})}{V_0} - f_0 \leq 0, \tag{2.1c}$$

$$0 \leq \rho_{\min} \leq \rho \leq 1, \tag{2.1d}$$

where c is the compliance, which is the objective to be minimized using the vector of design variables $\boldsymbol{\rho}$, which is a vector containing the densities of all the finite elements. $\mathbf{U}$ is the global displacement vector and $\mathbf{K}$ is the global stiffness matrix. $\mathbf{F}$ is the global force vector, $\mathbf{u}_e$ is the element displacement vector and $\mathbf{k}_0$ is the element stiffness matrix. $V(\rho)$ and V_0 are the volume of the intermediate design and the design domain volume. f_0 is the prescribed volume fraction, $\rho_{\min}$ is a scaler of a minimum density to avoid singularity and p is the penalization factor introduced to ensure black-white solutions.

Optimization problems can be solved using several different algorithms, such as Optimality Criteria (OC) methods, Sequential Linear Programming (SLP) and the Method of Moving Asymptotes (MMA) [20]. In this thesis, both OC and MMA are used for optimization [24]. This entire optimization procedure has been made available as an easy to read MATLAB code by Sigmund [20]. This code was later made more efficient and shorter by Andreassen et al. which resulted in the 88 line code [1], which is used as a basis in this thesis.

Some problems might arise if optimization is done as described above. An example of a problem is checkerboard patterns [23],. However, this is unrealistic and nearly impossible to manufacture. For that reason, filtering techniques are used. The density filter introduced by Bruns and Tortorelli [5] is one of the most common techniques used which both eliminates checkerboard patterns as well as imposes a length scale which cancels out one or two node hinges. The density filter transforms the original densities ρ_e as follows,

$$\tilde{\rho}_e = \frac{1}{\sum_{i \in N_e} H_{\text{ei}}} \sum_{i \in N_e} H_{\text{ei}} \rho_i, \tag{2.2}$$

where N_e is the set of elements i for which the centre-to-centre distance $\Delta(e,i)$ to element e is smaller than the predefined filter radius $r_{\min}$. The weight factor, H_{ei}, is defined as follows,

$$H_{\text{ei}} = \max\left(0, r_{\min} - \Delta(e,i)\right). \tag{2.3}$$

The sensitivities of the objective function c and the density V with respect to the design variables ρ_j are given as follows,

$$\frac{\partial \psi}{\partial \rho_j} = \sum_{e \in N_j} \frac{\partial \psi}{\partial \tilde{\rho}_e} \frac{\partial \tilde{\rho}_e}{\partial \rho_j} = \sum_{e \in N_j} \frac{1}{\sum_{i \in N_e} H_{ei}} H_{je} \frac{\partial \psi}{\partial \tilde{\rho}_e}, \tag{2.4}$$

where ψ is either the objective or the volume function. The 88 line code includes a sensitivity filter as well as a density filter [1]. To reduce the number of lines and memory requirements, the filtering is done using the CONV2 function in MATLAB, which is mathematically equivalent to the above mentioned formulas.

2.2. Topology optimization of compliant mechanisms

Compliance minimization is the most common problem used in TO literature. However, to design a compliant mechanism (CM), a different objective must be chosen. A CM obtains its motion from the flexibility of its members and thus the part must not be too stiff. There are two main groups of objective functions which can be chosen, the first of which is established by treating the design as a multi-objective problem, where the compliance and stiffness are both optimized. Usually, a ratio between the two is chosen, which can be altered to one's preference. The second group of objectives is one where a mechanical measurement is chosen to be optimized, this can be flexibility, geometrical advantage (GA), mechanical advantage (MA) or output displacement [6] [30]. As mentioned by Zhu et al. [30], the output displacement has become a common choice for the objective function. Therefore, output displacement will be used as the objective in this thesis. CM

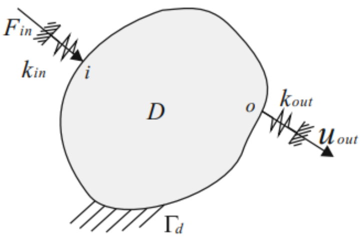

Figure 2.2: General design domain for compliant mechanisms, where F_{in} is the input force at input port i and at output port u, output displacement u_{out} is desired. Springs are attached to both the input port and the output port, as seen by k_{in} and k_{out}. D is the design domain and Γ_d is the region where the boundary conditions are applied. [29]

design problems have additional constraints, for example, input and output displacement limits. The input displacement constraint can be realized by adding a spring k_{in} at the input port. A spring k_{out} is attached to the output port to imitate the resistance from the workpiece, which is known as the spring model [30]. An example of the general design domain can be seen in Fig. 2.2, where F_{in} is the input force at input port i and at output port u, output displacement u_{out} is desired. Springs are attached to both the input port and the output port, noted as k_{in} and k_{out}, respectively D is the design domain and Γ_d is the region where the boundary conditions are applied. The TO problem for designing CM can be written as follows,

$$\min_{\rho} \qquad -u_{\text{out}}, \tag{2.5a}$$

$$\text{Subject to} \qquad \mathbf{KU} = \mathbf{F}, \tag{2.5b}$$

$$\frac{V(\boldsymbol{\rho})}{V_0} - f_0 \leq 0, \tag{2.5c}$$

$$0 \leq \rho(x) \leq 1. \tag{2.5d}$$

Compared to the compliance minimization TO problem, the objective is the maximization of displacement at the output port, which is equivalent to the minimization of $-u_{\text{out}}$. Another change is that a dummy load is added in the direction of the desired output displacement. This means a second displacement vector must be calculated. Both displacement vectors are then used in the calculations of the sensitivity of the objective function.

2.2.1. Sensitivities

The sensitivity of the objective function is given as,

$$\frac{\partial u_{\text{out}}}{\partial \rho_e} = p\rho_e^{p-1}\left(E_0 - E_{\text{min}}\right) u_{\text{Fin,e}}^{\text{T}} k_0 u_{\text{Fout,e}}, \tag{2.6}$$

where $u_{\text{Fin,e}}$ and $u_{\text{Fout,e}}$ are the displacements of element e due to the input force and the dummy force. E_{min} is small stiffness assigned to void regions, so that the stiffness matrix does not become singular and E_0 is the stiffness of the material. The sensitivity of the volume with respect to the design variable is as follows,

$$\frac{\partial V}{\partial \rho_e} = 1, \tag{2.7}$$

because of the linear relation between element density and volume.

2.3. Robust design

As mentioned in Section 2.2, a penalty scheme is used to obtain a black/white crisp result from the TO and a filter is used to avoid checkerboard patterns. There is however a drawback, as the resulting design will consist of grey transition areas between the solid and void regions. These grey transition areas have a density which is not zero or one, which is a problem as it is very difficult to manufacture. One possible solution to this problem is using projection methods, whereby each iterative solution is projected to a 0–1 design using, for example, the Heaviside projection method. This method does solve the issue of grey transition areas, but it destroys the length scale imposed by the density filter, which will result in one or two-node hinges. A method which uses a projection method and ensures local mesh-convergence, is called the robust method [27].

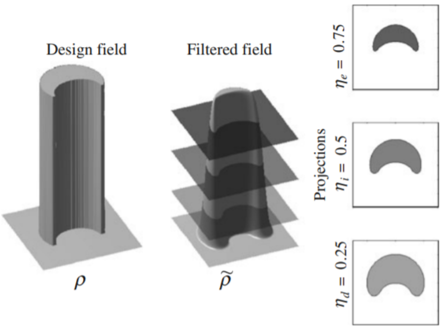

Figure 2.3: Threshold projection results for threshold value η [27]

2.3.1. Method

The robust method was originally developed to account for geometric variations due to manufacturing inaccuracies. It uses three different projections, a dilated $\bar{\tilde{\rho}}^d$, an intermediate $\bar{\tilde{\rho}}^i$ and an eroded $\bar{\tilde{\rho}}^e$ design. All three designs are used in the TO to ensure global and local mesh-convergence. The designs are formulated using three different projection thresholds, η, 0.5 and $1-\eta$, respectively. The three different projections can be seen in Fig. 2.3. Optimizing three designs also means the design problem has changed, the new design problem can be written as:

$$\min_{\rho} \quad \max\left(-u^e_{\text{out}}, -u^i_{\text{out}}, -u^d_{\text{out}}\right), \tag{2.8a}$$

$$\text{Subject to} \quad \mathbf{K}\left(\bar{\tilde{\rho}}^e\right)\mathbf{u}^e = \mathbf{f}, \tag{2.8b}$$

$$\mathbf{K}\left(\bar{\tilde{\rho}}^i\right)\mathbf{u}^i = \mathbf{f}, \tag{2.8c}$$

$$\mathbf{K}\left(\bar{\tilde{\rho}}^d\right)\mathbf{u}^d = \mathbf{f}, \tag{2.8d}$$

$$\frac{V(\boldsymbol{\rho})}{V_0} - f_0 \leq 0, \tag{2.8e}$$

$$0 \leq \rho(x) \leq 1. \tag{2.8f}$$

The optimization problem is now a min-max problem and will result in a very small amount of grey area while maintaining the same topology as without the robust method. The volume constraint is imposed on the dilated design and every 20 iterations, the volume fraction is updated so that the volume of the intermediate design becomes equal to the prescribed volume fraction which can be written as follows,

$$V_d^* = \frac{f_0}{V_i} V_d, \tag{2.9}$$

where V_d^* is the updated volume fraction of the dilated design, f_0 is the prescribed volume fraction, V_i is the volume fraction of the intermediate design and V_d is the volume fraction of the dilated design. The threshold projection is given as follows,

$$\bar{\tilde{\rho}}_i = \frac{\tanh(\beta\eta) + \tanh\left(\beta\left(\tilde{\rho}_i - \eta\right)\right)}{\tanh(\beta\eta) + \tanh(\beta(1-\eta))}, \tag{2.10}$$

where β is the projection parameter, with the maximum set to $\beta_{\max} = 128$. The initial value for $\beta = 1$ and is doubled every 50 iterations if it does not succeed $\beta_{\max}$, η is the threshold projection value. Fig. 2.4 shows the resulting projections using Equation 2.10 for $\beta = 1, \beta = 8, \beta = 3$ and $\beta = 128$. It clearly shows how the threshold projection gets stricter with increasing β value.

2.3.2. Sensitivities

The sensitivities of the objective with respect to the design variables can be calculated using the chain rule as follows [27]:

$$\frac{\partial f}{\partial \rho_j} = \sum_{i \in N_{e,j}} \frac{\partial f}{\partial \bar{\tilde{\rho}}_i} \frac{\partial \bar{\tilde{\rho}}_i}{\partial \tilde{\rho}_i} \frac{\partial \tilde{\rho}_i}{\partial \rho_j}, \tag{2.11}$$

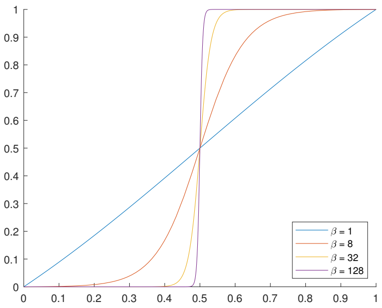

Figure 2.4: Threshold projection function for $\beta = 1, \beta = 8, \beta = 3$ and $\beta = 128$

where the first part is the sensitivity of the objective with respect to the physical design variables, which can be calculated as

$$\frac{\partial f}{\partial \bar{\tilde{\rho}}} = -p\bar{\tilde{\rho}}^{p-1} \left(E_0 - E_{\text{min}}\right) \mathbf{u}_e^{\mathrm{T}} \mathbf{k}_0 \mathbf{u}. \tag{2.12}$$

The second part of Eq. 2.11 is the threshold projection with respect to the filtered variable, which can be calculated as

$$\frac{\partial \bar{\tilde{\rho}}_i}{\partial \tilde{\rho}_i} = \frac{\partial}{\partial \tilde{\rho}_i} \left(\frac{\tanh(\beta\eta) + \tanh(\beta(\tilde{\rho}_i - \eta))}{\tanh(\beta\eta) + \tanh(\beta(1-\eta))} \right), \tag{2.13}$$

which can be rewritten to

$$\frac{\partial \bar{\tilde{\rho}}_i}{\partial \tilde{\rho}_i} = \frac{1}{\tanh(\beta\eta) + \tanh(\beta(1-\eta))} \left(\frac{\partial}{\partial \tilde{\rho}_i} \tanh(\beta(\tilde{\rho}_i - \eta)) \right), \tag{2.14}$$

which in turn can be rewritten to

$$\frac{\partial \bar{\tilde{\rho}}_i}{\partial \tilde{\rho}_i} = \frac{1}{\tanh(\beta\eta) + \tanh(\beta(1-\eta))} \left(\beta \operatorname{sech}^2(\beta(\tilde{\rho}_i - \eta)) \right). \tag{2.15}$$

The third part of Eq. 2.11 is the derivative of the filtered density with respect to the design variables, which can be calculated as

$$\frac{\partial \tilde{\rho}_i}{\partial \rho_j} = \frac{w(\boldsymbol{x}_j) v_j}{\sum_{j \in N_{e,i}} w(\boldsymbol{x}_j) v_j}. \tag{2.16}$$

2.4. Topology optimization with hotspot detection

As discussed, overheating during laser PBF printing is a big problem. Numerical models can help identify the issues and solve them, but detailed models are computationally heavy and for that reason they are impractical to couple them with TO. Ranjan et al. [17] introduced a computationally low-cost method which prevents AM-associated local overheating in TO designs by imposing a thermal constraint [18][17]. The method is inspired by the actual physics of the printing process and detects zones prone to local overheating.

2.4.1. Simplifications

Simplifications are necessary for reducing the computational time. The simplified model is found to be computationally fast while correctly predicting the zones of local overheating. Simplifications considered for hotspot detection are listed as follows:

1. A localized steady-state analysis is done, instead of a transient analysis
2. The interface between the solid and powder region of the design is assumed to be insulating as conduction through the powder is neglected
3. Convection and radiation from the top surface are neglected
4. It is assumed that the entire top layer is simultaneously exposed to the laser and therefore simultaneously exposed to the heat flux

5. Phase transformations are not considered

6. Material properties are assumed to independent of the temperature

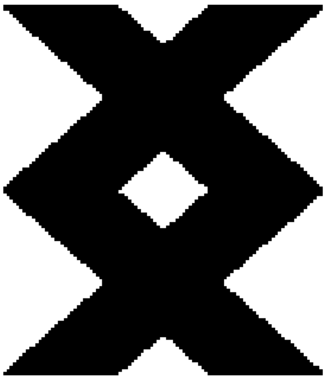

Figure 2.5: The design which is analysed using the hotspot method

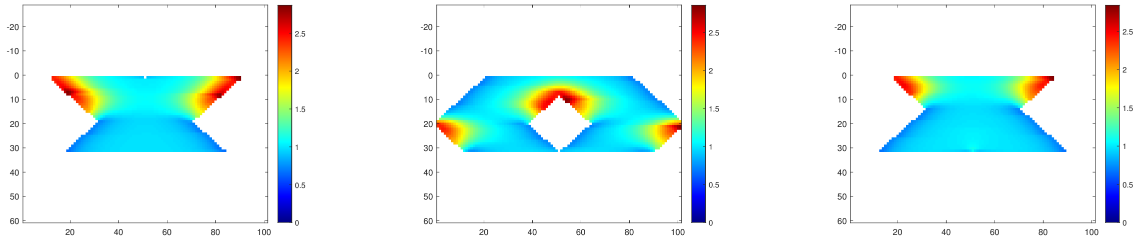

Figure 2.6: A design analysed with a different slab each time, first slab is near the bottom of the design, second slab is in the middle of the design and third slab is near the top of the design

2.4.2. Method

The method used was first introduced by Ranjan et al. [18], where it was shown that a steady-state analysis applied on a localized domain close to the heat source is capable of correctly predicting overheating zones. For this reason, the AM model which is integrated with TO considers only a subset of the geometry near the incident heat flux. This implies that the heat sink boundary condition is not located at the bottom of the entire domain, it is instead located at the bottom of a selected subdomain. This subdomain is referred to as a *slab*, with a slab thickness s. Fig. **??** shows a design analysed with a different slab each time. The domains of subsequent slabs largely overlap when the slab is passed through the design in the build direction, so that each element is analysed multiple times belonging to different slabs. The maximum temperature at each location from all the slabs is put together, which is called the temperature field or hotspot map. The maximum temperature of the hotspot map is used to normalize the temperature fields between 0 and 1. An example of a hotspot map, where all the analysed slabs are combined, can also be seen in Fig. 2.7.

2.4.3. Finite element implementation

The domain is discretized with a structured mesh of bi-linear four-node square elements. The elemental conductivity is given as

$$k_e = k_{\min} + (k_0 - k_{\min})\,\tilde{\rho}_e^r, \tag{2.17}$$

where k_e is the thermal conductivity for element e and k_0 is the thermal conductivity associated with bulk material. $k_{\min}$ is defined to avoid singularity and r is the penalization factor identical to the SIMP formulation

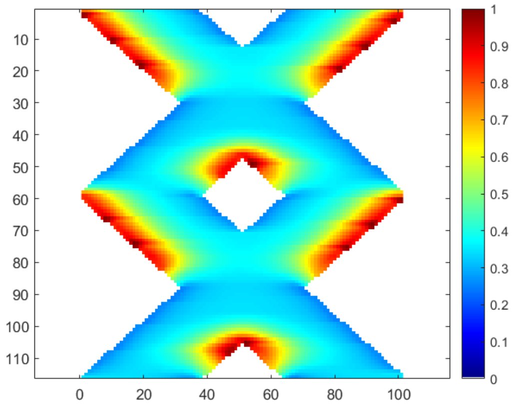

Figure 2.7: The design which is analysed using the hotspot method

[4]. The heat flux applied to element e is calculated as follows,

$$q_e = q_0 \tilde{\rho}_e^r, \tag{2.18}$$

where q_0 is the input heat flux. Using the elemental values for conductivity and flux, both global conductivity matrix $\mathbf{G}$ and thermal load vector $\mathbf{Q}$ can be assembled using standard assembling procedures in FEA [7]. The resulting steady-state heat equation is given as

$$\mathbf{G}^{(J)}\mathbf{T}^{(J)} = \mathbf{Q}^{(J)} \quad \forall \quad J \in [1, m], \tag{2.19}$$

where $\mathbf{T}^{(J)}$ are the nodal temperature vectors for each slab, with J being the slab index and m is the total number of slabs. The temperature is then normalized using $N_c = q_0 s/k_0$, which is the top surface temperature of a solid slab. Comparing the obtained temperatures with a solid slab gives it a physical meaning. This is done using

$$\tilde{\mathbf{T}}^{(J)} = \frac{\mathbf{T}^{(J)}}{N_c}. \tag{2.20}$$

Finally, the maximum temperature at each node is selected to obtain the hotspot map of the entire design using

$$\tilde{\mathbf{T}}^{\Omega_D} = \sum_{J=1}^{m} \mathbf{L}^{(J)}\tilde{\mathbf{T}}^{(J)}, \tag{2.21}$$

where $\mathbf{L}^{(J)}$ is a matrix prepared for the J^{th} slab to sequentially place all elements of $\tilde{\mathbf{T}}^{(J)}$ in $\tilde{\mathbf{T}}^{\Omega_D}$. The temperature values of all nodes should remain below a critical value, i.e. $\max(\tilde{\mathbf{T}}) \leq T_{cr}$. This max operator is not differentiable, but a smooth operation is required for calculating the sensitivities needed in TO. For this reason, a P-mean aggregation scheme is used. First a vector $\mathbf{g}$ is defined using

$$\mathbf{g} = \frac{\tilde{\mathbf{T}}^{\Omega_D}}{T^{\mathrm{cr}}}, \tag{2.22}$$

where $\tilde{\mathbf{T}}^{\Omega_D}$ is a vector in which the temperatures from all slabs $\mathbf{T}^{(J)}$ are combined in a single vector. After that, P-mean aggregation is used over the entire vector $\mathbf{g}$ to define the overheating constraint as follows,

$$f = \left[\frac{1}{n}\sum_{i=1}^{n} g_i^P\right]^{\frac{1}{P}} - 1 \leq 0, \tag{2.23}$$

where n is the total number of nodes in all the slabs belonging to the design domain, g_i is the i^{th} component of vector g and P is the exponent used for defining P-mean.

2.4.4. TO integration

Implementing the hotspot constraint in a standard compliance minimization TO results in the following optimization problem:

$$\min_{\rho} \quad c(\boldsymbol{\rho}) = \mathbf{U}^T\mathbf{K}\mathbf{U}, \tag{2.24a}$$

$$\text{Subject to} \quad \frac{V(\boldsymbol{\rho})}{V_0} - f_0 \leq 0, \tag{2.24b}$$

$$\left[\frac{1}{n}\sum_{i=1}^{n} g_i^P\right]^{\frac{1}{P}} - 1 \leq 0, \tag{2.24c}$$

$$\mathbf{G}^{(J)}\mathbf{T}^{(J)} = \mathbf{Q}^{(J)}, \tag{2.24d}$$

$$\mathbf{K}\mathbf{U} = \mathbf{F}, \tag{2.24e}$$

$$0 \leq \rho(x) \leq 1. \tag{2.24f}$$

The critical temperature is defined by a calibration step in which overhang angles are used, interested readers are referred to Ranjan et al. [17]. This thesis uses different values for the critical temperature by varying the associated overhang angle. This does not imply that an overhang avoidance scheme is used, rather, overhang angles are used to determine critical temperatures.

3

Case study evaluation

This chapter introduces the case which uses standard topology optimization (TO) for compliant mechanisms (CMs) without any hotspot constraint, displays the generated designs and evaluates the chosen design, which will be used in the next chapters.

3.1. Case study definition

Complex compliant mechanisms (CMs) are mainly designed using topology optimization (TO), which is why the goal here is to generate a CM, in this case a gripper, using TO. The resulting design will be evaluated with respect to overheating during the printing of the mechanism. It is decided to choose a design which has both thin and thick members so that the effect of the different members can be evaluated. As mentioned in chapter 2, multiple methods can be used to generate a compliant gripper. In this thesis, the 88-line code presented by Andreassen et al. [1] was altered to create a CM TO code. The code was altered to use the Method of Moving Asymptotes (MMA) as optimization scheme, instead of the standard optimality criteria [24]. This was done as it is known to work best for structural optimization problems [2].

3.2. Problem definition

TO is carried out using normalized physical quantities, since the problem is linear. For this reason, units are omitted, as is common in TO studies. The design domain is rectangular and has multiple passive elements as can be seen in figure 3.1. The two black boxes are solid blocks, they are to remain filled in during the optimization. These elements are placed in the design domain for better handling e.g., mounting during experimentation for accessing the functionality. The grey box is a void region, which ensures room for placing the object that needs to be gripped. The input force is positioned at the upper left corner and the output force is positioned at the bottom right corner, slightly above the grey box. Springs with stiffness $k_s = 0.01$ are attached to both the input force position and the output force position to limit the input displacement and to imitate the resistance from the object which is to be gripped. A symmetric boundary condition is applied to the complete bottom side as the design domain is only half of a gripper. Lastly, the solid box in the bottom left corner is fixed on the left side in both the horizontal and vertical direction.

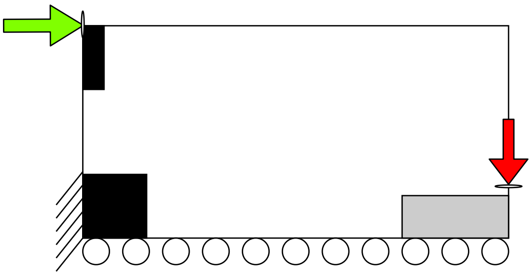

Figure 3.1: Design domain of the case study with black and grey boxes, where black is solid material and grey is a void area.

3.3. Optimization problem

Using the information from the previous section, the complete optimization problem can be given as follows,

$$\min_{\rho} \quad -u_{\text{out}}, \tag{3.1a}$$

$$\text{Subject to} \quad \mathbf{KU} = \mathbf{F}, \tag{3.1b}$$

$$\frac{V(\boldsymbol{\rho})}{V_0} - f_0 \leq 0, \tag{3.1c}$$

$$0 \leq \rho(x) \leq 1, \tag{3.1d}$$

where the objective is to maximize the output displacement at the point where the output force is located. An explanation of the above mentioned equations, the sensitivities and the filters used can be found in the previous chapter. In this chapter, the robust design method is not used.

3.4. Parameters

The last part which needs to be determined, before any optimization can be done, are the parameters used in the optimization. As mentioned before, units are omitted in this study. The parameters can be divided into two categories, the first category has parameters which are chosen before any optimization has been done and are not to be changed. These parameters are called constant parameters and can be seen in table 3.1. The stiffness of the material E_0 is one and the stiffness of void regions E_{min} is 10^{-6} to prevent singularity. The number of elements in the x direction n_x is 160 and the number of elements in the y direction n_y is 80, as the entire design domain is half of a gripper, thus the entire gripper is 160 × 160 elements. The SIMP penalty factor p is 3. The variable properties which can be chosen are the volume fraction f_0 and the filter radius r_{min}.

Table 3.1: Constant parameters

Parameter	Value
E_0	1
E_{min}	10^{-6}
n_x	160
n_y	80
p	3

3.5. Generated designs

Multiple designs have been generated using the above mentioned constant variables and varying either the filter radius or volume fraction. The different volume fractions chosen were: 0.2, 0.3, 0.4 and 0.5 and the different filter radii were: 1.5, 2, 3 and 6. The stopping criteria in the optimization depended on the number of iterations and the change per iteration. If the number of iterations were over 1000, the optimization would stop as the changes at that point were very minimal. If the change per iteration was below 0.001, the optimization would also stop. The change per iteration is calculated as the mean of the absolute values of the difference between the updated design variables and the previous design variables. The resulting figures obtained from the optimization can be seen in Figs. 3.2 – 3.5, where the volume fraction is constant in the horizontal direction and the filter radius is changed from 1.5 – 6. The resulting absolute objective values for

Table 3.2: Objective value (Gripper output displacement, larger is better) for the reference case for volume fraction ranging from 0.2 – 0.5 and filter radius ranging from 1.5 – 6

Volume fraction \filter radius	1.5	2	3	6
0.2	31.3764	31.0083	29.4050	24.4861
0.3	35.2606	34.8870	34.2480	32.0211
0.4	36.8499	36.8659	36.9603	35.5611
0.5	37.6550	37.6168	37.5728	36.8267

(a) $r_{\text{min}} = 1.5$ (b) $r_{\text{min}} = 2$ (c) $r_{\text{min}} = 3$ (d) $r_{\text{min}} = 6$

Figure 3.2: Generated designs with volume fraction $f_0 = 0.2$ and varying filter radius $r_{\text{min}} = 1.5, 2, 3$ and 6

(a) $r_{\text{min}} = 1.5$ (b) $r_{\text{min}} = 2$ (c) $r_{\text{min}} = 3$ (d) $r_{\text{min}} = 6$

Figure 3.3: Generated designs with volume fraction $f_0 = 0.3$ and varying filter radius $r_{\text{min}} = 1.5, 2, 3$ and 6

(a) $r_{\text{min}} = 1.5$ (b) $r_{\text{min}} = 2$ (c) $r_{\text{min}} = 3$ (d) $r_{\text{min}} = 6$

Figure 3.4: Generated designs with volume fraction $f_0 = 0.4$ and varying filter radius $r_{\text{min}} = 1.5, 2, 3$ and 6

(a) $r_{\text{min}} = 1.5$ (b) $r_{\text{min}} = 2$ (c) $r_{\text{min}} = 3$ (d) $r_{\text{min}} = 6$

Figure 3.5: Generated designs with volume fraction $f_0 = 0.5$ and varying filter radius $r_{\text{min}} = 1.5, 2, 3$ and 6

all optimizations can be seen in table 3.2, where the volume fraction is changed in the vertical direction and the filter radius is changed in the horizontal direction.

3.6. Chosen design

The resulting designs were compared and as expected, a higher volume fraction resulted in a higher objective value. The goal here is not to have an objective value as high as possible but rather have a design which has features which can be evaluated with respect to the overheating during printing. A volume fraction of 0.3 and a filter radius of 6 were chosen as final parameters, as this design is not fragile and will therefore not completely fail during printing. A new optimization was done with an increased maximum number of iterations of 2500 to try to get an even better result for the same parameters. The resulting topology can be seen in figure 3.6. Note that its boundaries show the characteristic blurring of the density filtering, and that no single-node hinge has formed. In the next chapter, post-processing by thresholding this design will be performed as preparation for additive manufacturing and multiple experiments will be done.

Figure 3.6: Final chosen design obtained with topology optimization with filter radius $r_{\text{min}} = 6$, volume fraction $f_0 = 0.3$ and objective value 32.0211

4

Experiments

This chapter explains the steps which were taken to print the optimized designs and which physical and computational experiments were done on the design. The goal of the physical experiments was to find out if the grippers had the intended movement and the goal of the computational experiments was to validate the physical experiments and to find out if any area of the gripper had a chance of overheating during printing.

4.1. From MATLAB code to 3D design

The previous chapter explained how the reference case was designed, this was however only half of a 2D gripper. Instead of printing a full 2D gripper, the decision was made to print a 3D gripper made from three-half 2D grippers. This was done because printing a 3D gripper is more challenging than printing a 2D gripper as a 2D gripper could be printed facing the base plate, which would result in very few problems. The 2D design obtained from the topology optimization (TO) process was extruded in the out of plane direction with 10 elements as thickness, which was equivalent to 1.125 mm. This was also done on a test design which was printed in plastic at Penn State University, which gave satisfactory results. After that, the design was loaded into the TOPslicer application in MATLAB [28]. This application can transform a generated 3D topology in MATLAB into a STL file. TOPslicer uses a threshold of $\rho > 0.5$ to decide what part of the geometry is considered material or void. Densities above 0.5 are considered material and below 0.5 are considered void. The isosurface is the three-dimensional equivalent to the two-dimensional contour line. The isosurface is calculated using four-dimensional data, each element in the domain is associated with 3 coordinates and a single density. To ensure the closure of the isosurface, a layer of void elements is added next to the boundary of the domain. The surface is discretized into triangles that are directly outputted to an STL file.

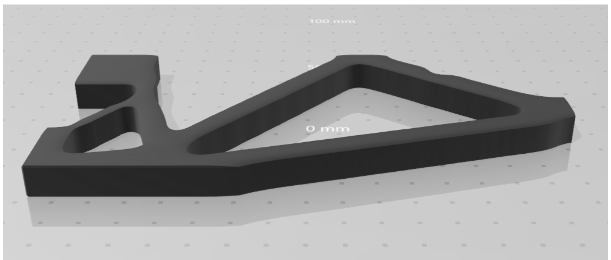

Figure 4.1: Design obtained after using TOPslicer application [28] to transform the MATLAB data into an STL file, which can be used to print the design

Fig. 4.1 shows the obtained half-gripper from the TOPslicer application. The STL file was then imported into SOLIDWORKS, which is a CAD modelling application. The thickness of the gripper was 1.125 mm, the height was 18 mm and the width was 9 mm. The application was used to build a 3D gripper consisting of three half-grippers. This was done by duplicating the half gripper and rotating it around the middle axis by 120 degrees. After that, the original half gripper was duplicated again and rotated by 240 degrees, resulting in a full 3D gripper as can be seen in Fig. 4.2. In total, three variations of the gripper were made. One with the original size, one with double the size and one with three times the original size. The reason for having

Figure 4.2: Design obtained after using the SOLIDWORKS application to transform the single arm design into a three-arm design

different sizes was to find out if there would be any differences in defects due to sizing. It was also done as it was not known what test equipment was going to be used to test the gripper, printing different sizes would mean the chance of having a correct size was higher.

4.2. From 3D design to printed gripper

The full 3D grippers from SOLIDWORKS were subsequently imported into Magics, which is a software application which prepares STL files for printing. The functionalities include STL repair/editing, support generation and placement on the baseplate. The support generation function was used and it resulted in support material near the bottom of the gripper, as pointed out by the red arrows in Fig. 4.3. The final Magics file was sent to 3D SYSTEMS, a printing company in Pennsylvania which has experience with printing metal CMs. The printer used was the ProX DMP 320 and the material used was Inconel 625, because CMs have been successfully printed using Inconel 625 [10] and because of the availability at 3D SYSTEMS. Multiple grippers for each size were printed so that multiple tests could be done. The smallest gripper was printed six times, the double size five times and the triple size 4 times due to available print area. The result can be seen in Fig. 4.3, with the three different size grippers and multiple other objects, which do not belong to this thesis. A heat treatment was done to release any residual stresses in the grippers. The grippers were removed from the base plate by wire Electrical Discharge Machining (EDM), removing a 1 mm layer from the bottom of all the grippers.

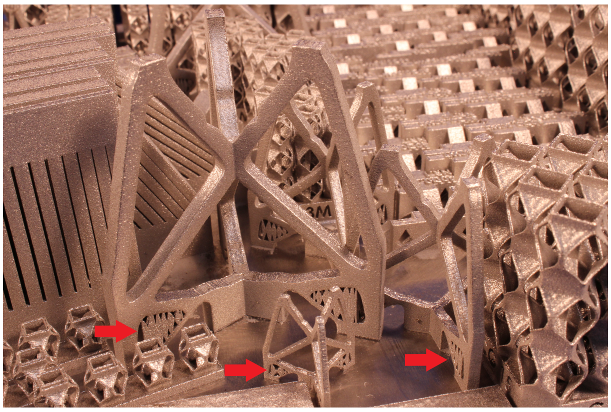

Figure 4.3: The three different size printed Inconel 625 grippers on the base plate before removal with red arrows pointing to the added support generated using the generation function of Magics

4.3. Hotspot analysis

The hotspot analysis method introduced in Sec. 2.4 was used to analyse the chosen design, after the same threshold of 0.5 as in the TOPslicer application was applied, to determine if any regions were at risk of overheating during printing. A 2D half gripper was analysed in the printed direction. The slab thickness s of 12 elements was used as in [17]. Later, in Sec. 5.3.2, a detailed discussion is given about the implications of this choice. The resulting temperature field can be seen in Fig. 4.4, where the maximum normalized temperature is 6.18. The maximum temperature is located at an area with a large overhang and a thin member of the gripper, at the same location where Magics automatically added support material before printing to ensure the gripper would not fail printing. This indicates that both methods can identify the region with the highest risk of overheating.

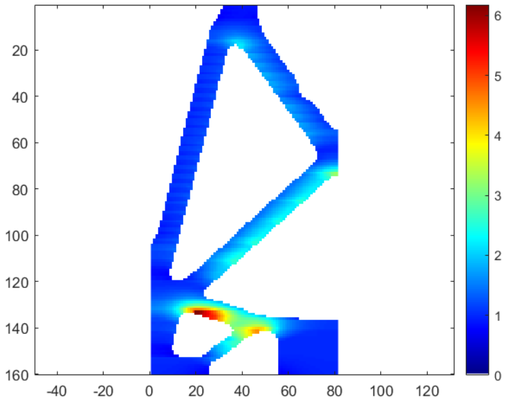

Figure 4.4: Temperature field of printed design with a maximum relative temperature of 6.18

4.4. Inspection of the printed grippers

The grippers were shipped to the Netherlands packaged in bubble wrap to make sure they would not get damaged. After arrival, a visual inspection was done to locate any visual defects on the grippers. The three different size grippers can be seen in Fig. 4.5, where the triple size gripper already had its support material removed. There were no visual defects on the triple size gripper, it was however noticed that the surface roughness was very high. The same observations were done for the double sized gripper. Surface roughness was very high for all three sizes on all the inside faces of the three triangles inside the gripper . Moreover, during wire-EDM of the smallest size gripper, significant amount of material from the bottom was removed. This is evident in Fig. 4.6. This resulted in a situation where it was extremely difficult to remove the support material without breaking the complete gripper. For this reason, the smallest gripper of the three variations has not been used in the mechanical tests.

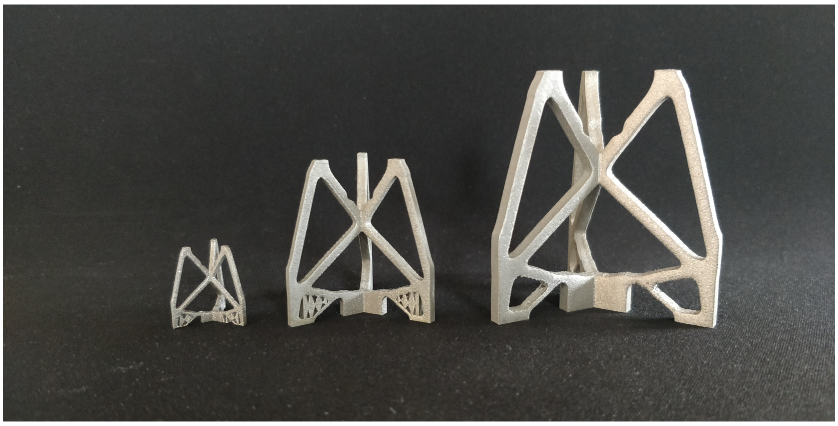

Figure 4.5: The three different size printed grippers with the support material removed for the biggest gripper

Figure 4.6: Smallest gripper in an upside down position to show the lack of material at the bottom of the gripper

4.5. Mechanical testing

Testing was done at the Technical University in Delft on the 7th of August 2020. The goal of the tests was to investigate if the grippers were functioning in the intended way and to find out if there were any internal defects due to overheating, which could have an impact on the strength and flexibility of the gripper. In total, five tests have been done using the double and triple size grippers. The smallest gripper was excluded from mechanical testing as it was impossible to remove the support material without breaking the gripper. The support material of the grippers was removed using a pair of pliers and the remaining little pieces of support material which were stuck on the grippers were removed using a smoothing file. The setup of the tests can be seen in Fig. 4.7. It was chosen to do a force-displacement test in the opposite direction than what the gripper was designed for. This was done as the available equipment for an experiment in the intended direction was not available and had to be completely made from scratch. By using force by hand it was obvious that the grippers were extremely stiff, for that reason it was chosen to only do an experiment with the available equipment, as that would not have given any new insight into overheating of the grippers during printing. The experiments consisted of a bar which had a constant displacement until the total displacement was reached, after that, the bar was released with a constant displacement until there was no remaining force on the gripper. The experiment had a fail-safe that would unload the bar at the moment the maximum amount of force was reached.

4.5.1. Double size gripper

Three experiments were done using the double size gripper variant, a maximum force of 500 N, 750 N and 1000 N was used as 1000 N was the maximum amount of force available during testing. The machine was set to move a maximum of 1 mm and to move at a speed of 1 mm/min. The resulting force-displacement data can be seen in Fig. 4.8. Only the test with a maximum of 1000 N could reach the full displacement of 1 mm and therefore complete a full cycle. The gripper had a very small displacement for the amount of force used as was expected because when applying force by hand the gripper did not move at all. It appears that at a relatively low force, a part of the gripper with lower stiffness is first compressed until that part has the same stiffness as the other parts of the gripper. It can also be noticed that there is plastic deformation starting at around 700 N, as can be seen by the 1000 N curve. At that moment the gripper undergoes permanent deformation as can be seen by the location where the slope ends up after releasing the applied force, located at 0.3 mm.

4.5.2. Triple size gripper

Considering the results of the double size gripper, only two experiments were done using the triple size gripper, for which a maximum force of 500 N and 1000 N were used. The same parameters were used as in the experiments with the double size gripper, namely, a maximum of 1 mm displacement at a speed of 1 mm/min. The resulting force-displacement data can be seen in Fig. 4.9. Both experiments did not reach the full 1 mm

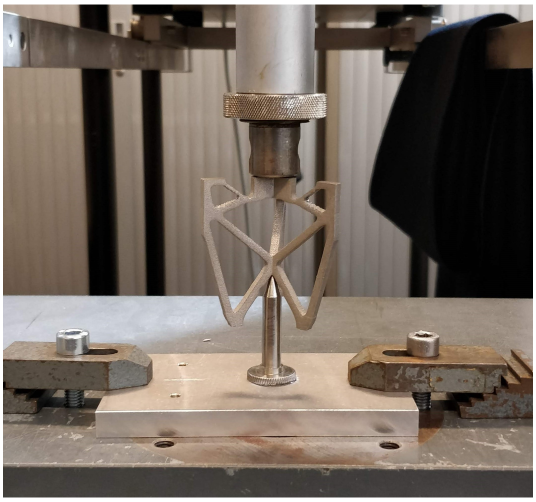

Figure 4.7: Mechanical test setup of the triple size gripper in the upside down position constraint using a pin. A downward force is applied on the bottom of the gripper

displacement as was expected looking at the results from the double size gripper. For future work, the physical experiments should be considered so the necessary equipment can be printed or pre-made, so that all experiments can be done.

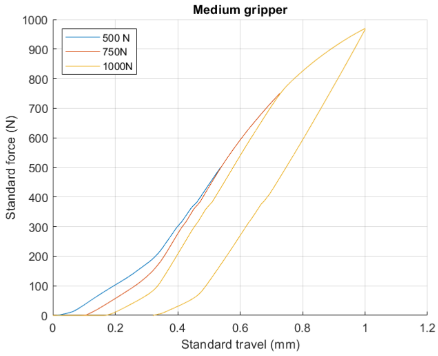

Figure 4.8: Double size gripper test results

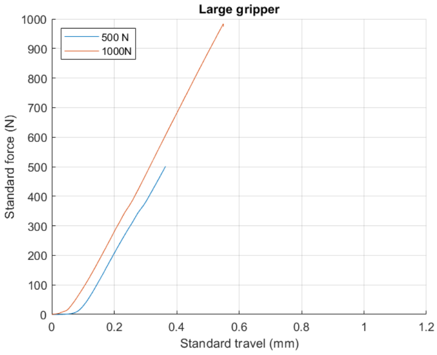

Figure 4.9: Triple size gripper test results

4.6. Mechanical simulation

Two different mechanical simulations have been done using COMSOL. The first simulation was done to investigate what the displacement field of the chosen design was using the boundary conditions of the design problem, to investigate the motion of the gripper. The second simulation was a replica of the mechanical experiment, to compare the output displacement and see if they would match. However, the STL could not be adequately processed in COMSOL. Due to the dangling surfaces in the STL, the three shapes could not be properly united to make one solid body needed for replicating the physical experiment. Due to this, it was decided to not perform the mechanical simulation for the entire 3D shape. Alternatively, a single arm was considered, that did not show these problems. A scaled down force was applied to recreate the physical experiment.

4.6.1. Design Problem

The 3D one arm design received from the TOPslicer application as can be seen in Fig. 4.1 was imported into COMSOL as an STL file. It was chosen to do a stationary study of the design with the same boundary conditions as the case study, which can be seen in Fig. 4.10. The material properties of Inconel 625 were used, which are the following: a Young's Modulus of 175 GPa, a Poisson's ratio of 0.3 and a density of 8440 kg/m^3. These values were received from tensile testing of test specimen on the same print job. A boundary load of

1000 N was applied at the input force location to give insight into the movement of the gripper, also, a *extra fine* element mesh was used. The resulting displacement field can be seen in Fig. 4.11, where the displacement is scaled by a factor 200 to show the motion of the gripper. The resulting displacement at the output force location was obtained by doing a point evaluation. The output displacement was 0.0383 mm in the positive x direction and 0.0142 mm in the positive y direction. To get some insight into what these values mean, MATLAB was used to do a displacement analysis using the material properties of Inconel 625 to see what the output displacement was for real values. The displacement at the output port was 0.0319 mm, comparing that to the 0.0142 mm of the COMSOL analysis, it can be concluded that the modifications done to obtain the STL file have had an influence on the output displacement and resulted in 55 % loss of output displacement.

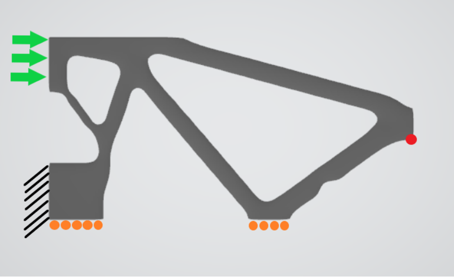

Figure 4.10: Boundary and loading conditions used for the design problem analysis using COMSOL, where the green arrows indicate the location of the applied force, the red dot the output location, the orange dots a roller constraint and the black bars a fixed constraint

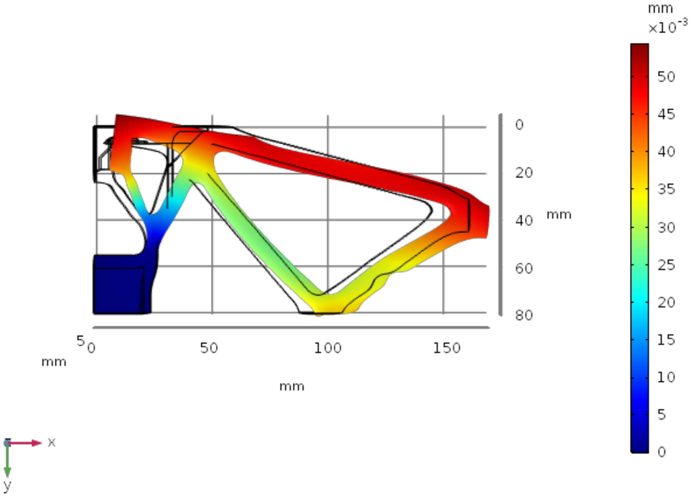

Figure 4.11: Resulting displacement field of the chosen design obtained in COMSOL by applying a force of 100 N at the top left corner in the positive x-direction

4.6.2. Replicating the physical experiment

The second simulation was done using the same Inconel 625 properties as in the first simulation.Fig. 4.12 shows the boundary and loading conditions applied replicating the physical experiment. The green arrows indicate the location of the applied boundary load of $\frac{1000}{3}$ N. Because one third of the entire printed gripper is used in the simulation, the force is divided by three to recreate a simulation as close to the real experiment. A fixed constraint is applied at the blue arrow to imitate the pin and the orange dots represents that area where a roller constraint is applied. The red dot indicates the output location. The resulting displacement field for the double and triple size grippers can be seen in Figs. 4.13 and 4.14. The resulting maximum displacement of the double size gripper at the point where the force is applied is 0.0512 mm in the positive X direction and for the triple size gripper, 0.0341 mm in the positive X direction. This is significantly lower than the resulting maximum displacement of the physical experiment, where the maximum displacement for the double size gripper was 1 mm for 969 N and for the triple size gripper, 0.55 mm as can be seen in Figs. 4.8

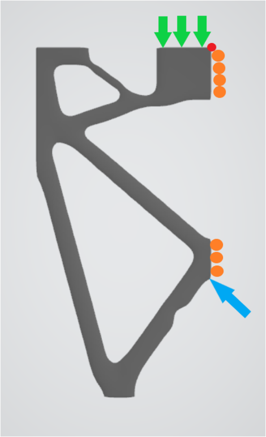

Figure 4.12: Boundary and loading conditions used for the design problem analysis using COMSOL, where the green arrows indicate the location of the applied force, the red dot the output location, the orange dots a roller constraint and the blue arrow, the location of the fixed constraint

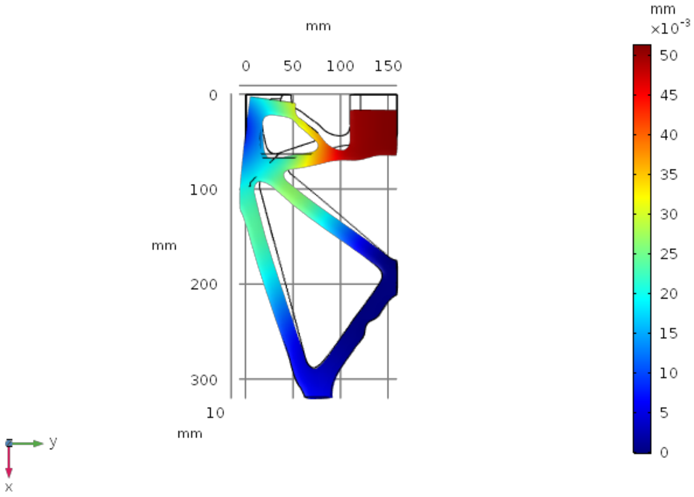

Figure 4.13: Resulting displacement field of the double size chosen design obtained in COMSOL by applying a force of $\frac{1000}{3}$ N at the top right corner in the positive x-direction, where the displacement is scaled by a large number to give insight in the movement of the gripper

and 4.9. In COMSOL, a linear analysis was done. Therefore, a force/displacement line can be made and plot together with the results from the physical experiment, so that they can be compared. Figs. 4.15 and 4.16 show these plots where it is noticeable that the COMSOL result is different than the result from the physical experiment. There is a significant difference between the experimental results and the simulation results. The COMSOL simulation shows a much stiffer gripper than the physical experiment. A possible reason for this is the fact that in the COMSOL simulation, the force is one third of the force during the physical experiment, however, the model is not completely one third. The reason for this is that the entire gripper is constructed of three half grippers and in the middle of the design, where the grippers are connected, the three half grippers overlap partly and thus less material is present than assumed in the COMSOL model. Other reasons for the large difference can be additional compliances in the measurement setup, misalignment in the test setup, or differences in material properties of the printed grippers. However, it cannot be ruled out that the regions that show the largest deformation, are significantly weakened in the experiment due to overheating effects in the printing process. Due to the limited access to the testing equipment, it was decided not to further investigate this difference.

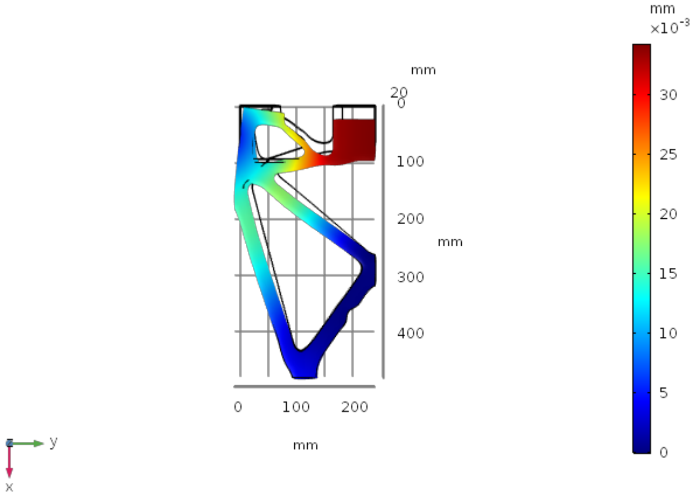

Figure 4.14: Resulting displacement field of the triple size chosen design obtained in COMSOL by applying a force of $\frac{1000}{3}$ N at the top right corner in the positive x-direction, where the displacement is scaled by a large number to give insight in the movement of the gripper

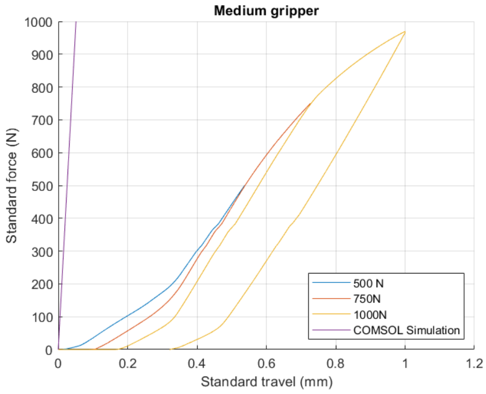

Figure 4.15: Double size gripper physical and COMSOL test results

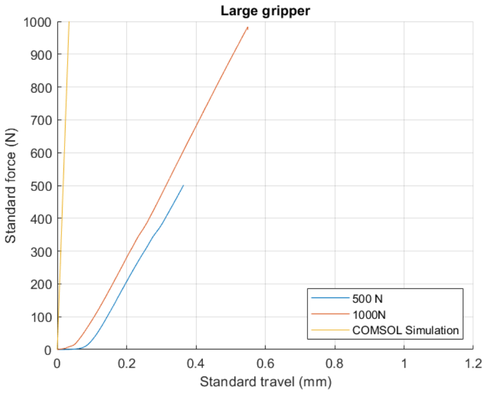

Figure 4.16: Triple size gripper physical and COMSOL test results

4.7. Conclusion

Multiple experiments have been done in this chapter, as well as simulations. The printed grippers did not show any visible defects due to overheating during printing and the hotspot method by Ranjan et al. [17] was able to identify a region at risk of overheating similar to the Magics software. The physical experiments showed that the grippers were very stiff, as they had barely any displacement for a force of 1000 N. The physical experiments also showed that before printing, the experiments should be considered so the necessary equipment can be printed at the same time.

The mechanical simulations showed a difference in output displacement compared to the physical experiments. There could be multiple reasons for this, the first simulation showed that the applied threshold had an influence on the performance of the grippers and the output displacement was reduced by 55%. The simulation of the physical experiment showed a much lower output displacement than the physical experiment. A possible reason for this is that the COMSOL model was not a complete reproduction of the physical experiment: multiple simplifications were taken to do the simulation. Also, the measurement and test setup could have had additional compliances or misalignments. Lastly, the local material properties of the printed grippers might have changed due to overheating during printing. This could not be proven but might be the reason for the large change in output displacement.

5

Topology optimization of compliant mechanisms with a hotspot constraint

This chapter introduces a new CMs optimization problem by adding a hotspot constraint. Several experiments are done using the new optimization problem and the effect of using the robust formulation is investigated.

5.1. Introduction

As explained in the previous chapter, no significant problems were discovered after printing of the reference case. However, as literature shows, overheating during printing is a big problem [8][12][16]. In this chapter, the same problem definition as in Chapter 4 is used to generate a compliant gripper. A hotspot constraint is introduced to prevent overheating during printing. The effect of multiple parameters is evaluated in this chapter. The quality of resulting designs is studied and a solution using the robust method is investigated.

5.2. Optimization problem

The hotspot constraint has been explained in Chapter 2. Adding the hotspot constraint to the CM optimization problem results in the following optimization problem:

$$\min_{\rho} \quad -u_{\text{out}}, \tag{5.1a}$$

$$\text{Subject to} \quad \frac{V(\boldsymbol{\rho})}{V_0} - f_0 \leq 0, \tag{5.1b}$$

$$\left[\frac{1}{n}\sum_{i=1}^{n} g_i^P\right]^{\frac{1}{P}} - 1 \leq 0, \tag{5.1c}$$

$$\mathbf{G}^{(J)}\mathbf{T}^{(J)} = \mathbf{Q}^{(J)}, \tag{5.1d}$$

$$\mathbf{KU} = \mathbf{F}, \tag{5.1e}$$

$$0 \leq \rho \leq 1. \tag{5.1f}$$

For the sensitivity of the hotspot constraint, interested readers are referred to the appendix.

5.3. Influence of parameters

The influence of different parameters on the resulting designs is examined in this section. The parameters considered are the critical temperature T_{crit}, slab thickness s, thermal penalization factor r and the part orientation. Some parameters are constant and have the same value as in the optimization done in Chapter 3. The filter radius $r_{\min}$ and volume fraction f_0 are the same as was used to obtain the chosen design. All default TO parameters are listed in Table 5.1 which are used, unless stated otherwise. The obtained temperatures are not real physical temperatures, they are indications of the risk of overheating.

Table 5.1: Constant parameters used in the optimization

Parameter	Value
E_0	1
E_{min}	10^{-6}
nelx	160
nely	80
p	3
r_{min}	6
f_0	0.3
s	12
r	9

5.3.1. Critical temperature

The critical temperature T_{crit} is a parameter which can be used to determine how strict the hotspot constraint is during the optimization, where a lower T_{crit} will result in a stricter constraint. Three different optimizations have been done using the parameters listed in Table. 5.1 with a critical temperature of $\tilde{T}_{\text{crit}} = 4.0$, $\tilde{T}_{\text{crit}} = 2.4$ and $\tilde{T}_{\text{crit}} = 1.7$ to investigate the effect of the critical temperature. The values of the critical temperatures are obtained by calibrating with overhang angles [17]. The topology obtained with the TO without hotspot constraint in Chapter 3 and the resulting topologies from varying the critical temperature can be seen in Figs. 5.1a – 5.1d. The main difference in topology comparing the new results to the original design is that the member near the bottom of the original gripper is now moved to the bottom plate and that the angle of the member in the middle of the design is changed. The overhang angle of that member increases for a lower T_{crit}, presumably because more heat must be conducted to satisfy the hotspot constraint. The objective has not changed by a large amount after introduction of the hotspot constraint, which implies that the addition of the hotspot constraint does not compromise performance. The temperature fields of the four topologies can be seen in Figs. 5.2a – 5.2d, where only temperatures of elements with densities greater than 0.3 have been visualized. This will be done for all the following temperature fields. The hotspot constraint is successful

(a) Resulting topology from CM TO without hotspot constraint with resulting output displacement $u_{\text{out}} = 32,0$

(b) Resulting topology from CM TO with hotspot constraint using $T_{\text{crit}} = 4$ with resulting output displacement $u_{\text{out}} = 31,4$

(c) Resulting topology from CM TO with hotspot constraint using $T_{\text{crit}} = 2.4$ with resulting output displacement $u_{\text{out}} = 31,2$

(d) Resulting topology from CM TO with hotspot constraint using $T_{\text{crit}} = 1.7$ with resulting output displacement $u_{\text{out}} = 30,5$

Figure 5.1: Resulting topologies with and without hotspot constraint in the printed orientation

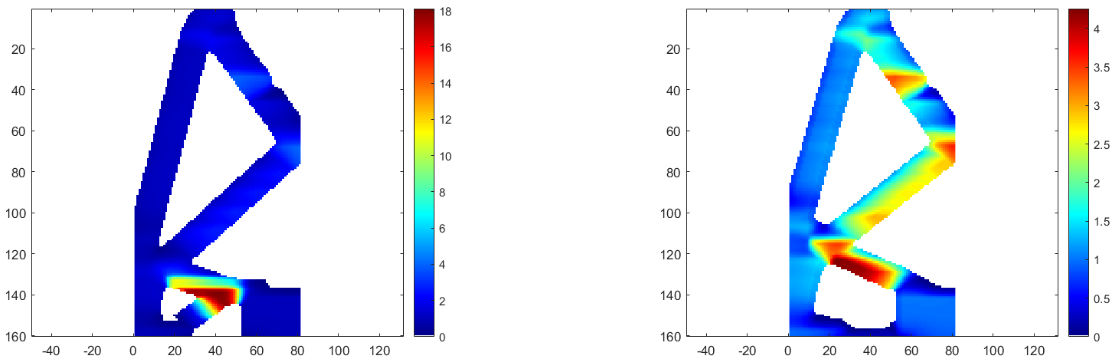

(a) Resulting temperature field from CM TO without hotspot constraint with a maximum temperature of 18, 1

(b) Resulting temperature field from CM TO with hotspot constraint with a maximum temperature of 4, 3, where $T_{\text{crit}} = 4$

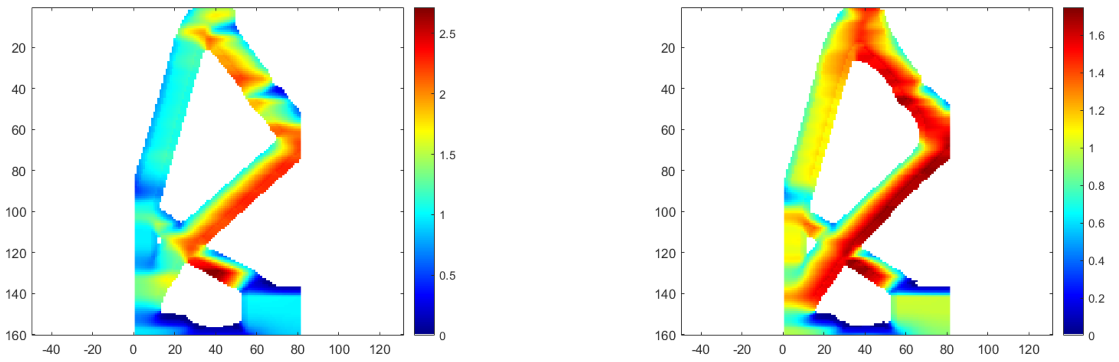

(c) Resulting temperature field from CM TO with hotspot constraint with a maximum temperature of 2, 7, where $T_{\text{crit}} = 2.4$

(d) Resulting temperature field from CM TO with hotspot constraint with a maximum temperature of 1, 7, where $T_{\text{crit}} = 1.7$

Figure 5.2: Resulting temperature fields obtained by hotspot analysis of the optimized designs

in limiting the maximum temperature for the three topologies designed with TO with a hotspot constraint, where the maximum temperature is near T_{crit} used in the optimization. Compared to the original design, the temperature is much lower and does not come close to the original maximum temperature. It can also be noted that as the constraint gets stricter, the entire design has almost the same temperature. When lowering the critical temperature T_{crit}, it will get even more difficult for the optimizer to find a solution. This implies that it becomes more and more difficult to find a solution as T_{crit} reduces.

5.3.2. Slab thickness

In this section, the influence of slab thickness s is analysed on the resulting designs. Three optimizations have been done with a slab thickness s of 5, 12 and 30. A critical temperature $T_{\text{crit}} = 2$ was used, as this was used by Ranjan et al. [17] and gave satisfactory results. The resulting topologies can be seen in Figs. 5.3a – 5.3c. There are almost no noticeable changes when comparing the three designs. However, as can be seen later in Sec. 5.6.6, with the robust formulation, the slab thickness does have an impact on the resulting topology. The resulting objective values also do not change much for different slab thicknesses. The resulting temperature fields can be seen in Figs. 5.4a – 5.4c. The same thresholding as above has been applied so that the temperature fields can be compared. An observation which can be made is that for a small slab thickness, higher temperatures arise along a specific side of the members, whereas for a larger slab thickness, the temperature is more spread out over the members. This might imply that smaller features which can have a large influence on the physical process are neglected when using a large slab thickness, which will result in worse representation of the actual process.

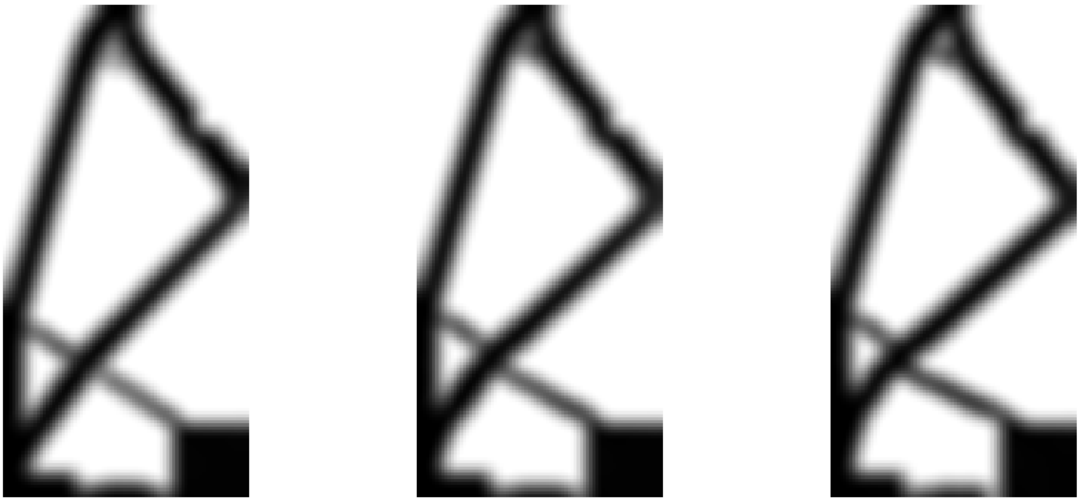

(a) Resulting topology from CM TO with hotspot constraint using slab thickness $s = 5$ with resulting output displacement $u_{\text{out}} = 30,8$

(b) Resulting topology from CM TO with hotspot constraint using slab thickness $s = 12$ with resulting output displacement $u_{\text{out}} = 31,0$

(c) Resulting topology from CM TO with hotspot constraint using slab thickness $s = 30$ with resulting output displacement $u_{\text{out}} = 31,2$

Figure 5.3: Resulting topologies for different slab thickness

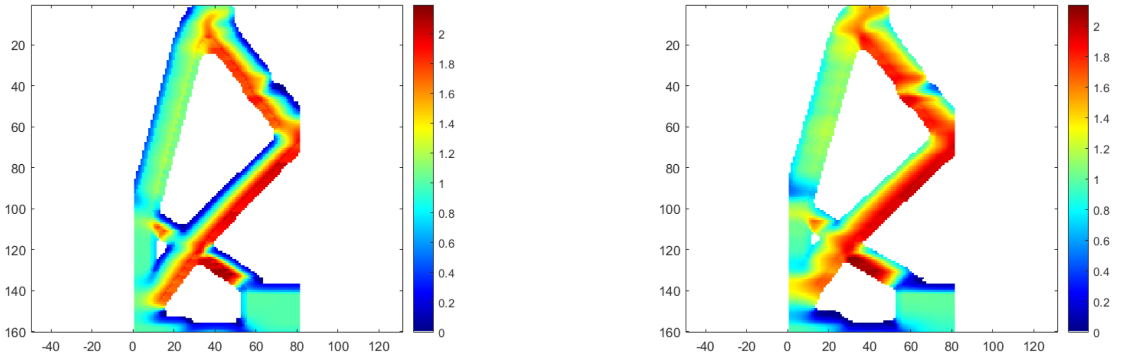

(a) Resulting temperature field from CM TO with hotspot constraint with a slab thickness $s = 5$, where $T_{\text{max}} = 2$

(b) Resulting temperature field from CM TO with hotspot constraint with a slab thickness $s = 12$, where $T_{\text{max}} = 2$

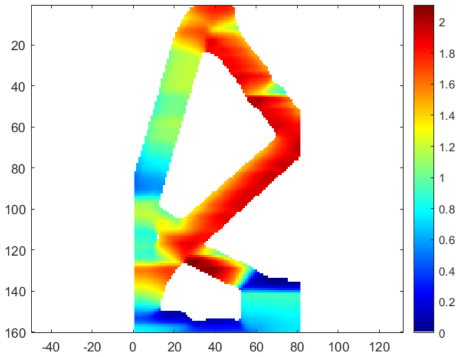

(c) Resulting temperature field from CM TO with hotspot constraint with a slab thickness $s = 30$, where $T_{\text{max}} = 2$

Figure 5.4: Resulting topologies for different slab thickness s

5.3.3. Thermal penalization factor

In this section, the influence of the thermal penalization factor r is evaluated. Three different optimizations have been done using a thermal penalization factor r of 3, 6 and 9. A slab thickness s = 12 and a critical temperature $T_{\text{crit}} = 2$ are used. The resulting topologies can be seen in Figs. 5.5a – 5.5c. It was mentioned that due to the design, changing the slab thickness had little influence on the resulting design. The same holds for the thermal penalization factor. Increasing the penalty factor would normally result in a decrease of intermediate densities, this is not the case for this design. However, as the design changes orientation or different boundary conditions are used, the thermal penalization factor may have an influence on the resulting topology. For that reason, the temperature fields of the designs in Figs. 5.5a – 5.5c will not be shown, as there is minimal difference. Later in the report more interesting differences due to the thermal penalization factor can be noticed.

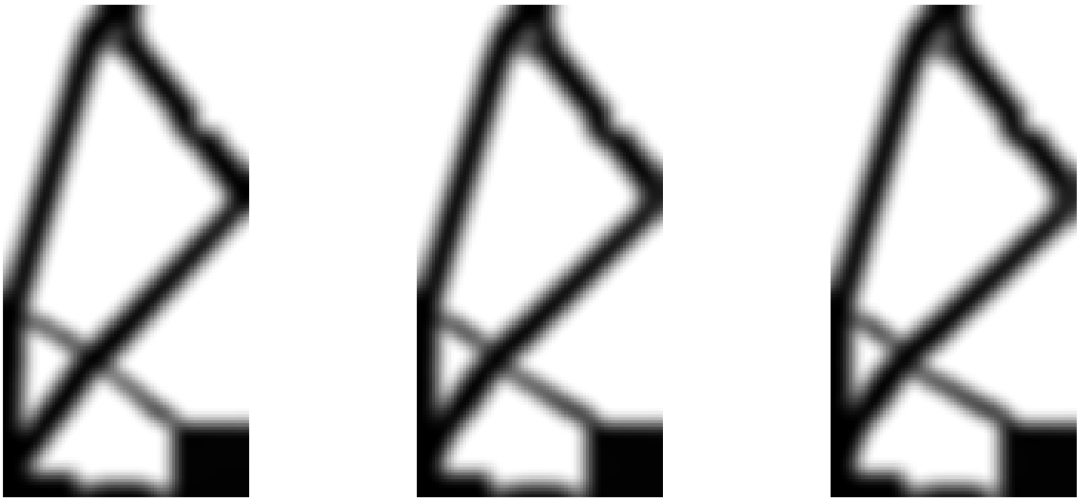

(a) Resulting topology from CM TO with hotspot constraint using thermal penalization factor $r = 3$ with resulting output displacement $u_{\text{out}} = 30,8$

(b) Resulting topology from CM TO with hotspot constraint using thermal penalization factor $r = 6$ with resulting output displacement $u_{\text{out}} = 31,0$

(c) Resulting topology from CM TO with hotspot constraint using thermal penalization factor $r = 9$ with resulting output displacement $u_{\text{out}} = 31,2$

Figure 5.5: Resulting topologies for different thermal penalization factors

5.3.4. Part orientation

In this section the part orientation will be discussed. Until now, only the printed orientation was used, but changing the orientation might give insight into a better orientation to print the design and show what parts of the design are critical with respect to the hotspot constraint. The parameters used are the same as in the optimizations above, a slab thickness $s = 12$, a critical temperature $T_{\text{crit}} = 2$ and a thermal penalization factor $r = 9$ are used. Four different print orientations will be used in the optimization, where the base plate is located at each of the four different sides of the design domain. Figs. 5.6a – 5.6d show the obtained designs where the blue bar in the figure represents the base plate. It is added to the figure to show the different orientations used. It can be observed that for the orientation with the base plate on the west side, the topology remains similar to the design obtained using the printed orientation. This is not the case for the two other orientations. The objective value is reduced by a lot more for the added three orientations compared to the printed orientation. However, all three added orientations have something in common, which are the big grey areas. As mentioned before, the grey areas cannot be produced as it is impossible to print intermediate densities. A threshold must be applied before any of these designs can be printed, but that would change the complete topology and the resulting objective value.

(a) Resulting topology from CM TO with hotspot constraint using the printed orientation with resulting output displacement $u_{\text{out}} = 31,0$

(b) Resulting topology from CM TO with hotspot constraint using the orientation with the base plate on west with resulting output displacement $u_{\text{out}} = 27,1$

(c) Resulting topology from CM TO with hotspot constraint using the orientation with the base plate on north with resulting output displacement $u_{\text{out}} = 24,1$

(d) Resulting topology from CM TO with hotspot constraint using the orientation with the base plate on east with resulting output displacement $u_{\text{out}} = 27,4$

Figure 5.6: Resulting topologies with hotspot constraint with different orientations where the blue bar shows the location of the base plate used in the optimization

5.4. Greyness problems

As seen in the results above, a large part of the design domain has a grey infill, which means it has an intermediate density between 0 and 1. This is not ideal, as this cannot be printed and so the resulting design is not as useful as desired. This is a common problem in topology optimization and normally a threshold is applied so that the design can be printed. Applying a threshold to a design optimized for stiffness is generally not a problem, as the compliance might change a little bit but that will not change the overall performance by a large amount. For compliant mechanisms, this is not the case, as small features enable the movement of the compliant mechanism. Therefore, even a small change can have a large effect. Sigmund [21] introduced a method of calculating the percentage of greyness called the measure of non-discreteness M_{nd}, which is calculated as follows,

$$M_{\text{nd}} = \frac{\sum_{e=1}^{n} 4\tilde{\rho}_e \left(1-\tilde{\rho}_e\right)}{n} \times 100\%, \tag{5.2}$$

where n is the number of elements and $\tilde{\rho}_e$ is the physical density for element e. If a design is fully converged to a 0–1 design, M_{nd} is 0 and for a design filled with intermediate densities, M_{nd} is 100. It is desired to have an as low as possible percentage so that the design will not change much after applying a threshold. The original design which was used to print the grippers has an M_{nd} of 30,0%, which is a high value of itself. The M_{nd} percentage of the four designs optimized using the different orientations can be seen in Table. 5.2. It can be noticed that the value increases a little after the introduction of the hotspot constraint for the printed orientation. For the other orientations, the percentage increases even more. This is not ideal. Lowering the filter radius has a large influence on the percentage of greyness. Therefore, a new optimization was done using a filter radius $r_{\text{min}} = 1.5$ using the printed orientation in the hotspot constraint. The resulting topology can be seen in Fig. 5.7a. It is observed that the design is much clearer and it appears there is a reduction in the amount of grey in the design. The percentage of greyness M_{nd} is 10,4 which is significantly lower than before. Also, the objective value has increased by 9.7%. A second optimization has been done using the east orientation from the section above. This case had the most issues with greyness, therefore this orientation was used to find out if decreasing the filter radius solved the greyness problems. The resulting topology can be seen in Fig. 5.7b, where the design is indeed much clearer but the greyness problems are not solved. The percentage of greyness M_{nd} is 26,9 which lower than for a higher filter radius but it is not good enough. A possible solution which was also tried was increasing the volume fraction so that there was more material for the optimizer to use to obtain a clear design. That did not solve the problem and therefore it was decided not to include it here. Since reducing the filter radius does not resolve the greyness problem, a new solution needs to be found to obtain printable solutions to the optimization problem for every orientation.

Orientation used	M_{nd}
Printed	30,6 %
West	36,3 %
North	36,0 %
East	40,9 %

Table 5.2: M_{nd} for the orientation used in the hotspot constraint

(a) Design obtained using $r_{\text{min}} = 1.5$ and the printed orientation with resulting output displacement $u_{\text{out}} = 34,0$

(b) Design obtained using $r_{\text{min}} = 1.5$ and the east orientation with resulting output displacement $u_{\text{out}} = 30,0$

Figure 5.7: Resulting topologies with hotspot constraint with different orientations where the blue bar shows the location of the base plate used in the optimization, with a lowered filter radius $r_{\text{min}} = 1.5$

5.5. Robust design method

Wang et al. [27] introduced a modified robust formulation which ensures black-white designs as an addition to the standard TO with a filter. The method can generate near perfect designs with a grey percentage M_{nd} of around 1. The details of the method are explained in Chap. 2. The modified robust formulation will be used in combination with the compliant mechanism TO code with hotspot constraint to obtain black-white designs. The updated optimization problem is as follows,

$$\begin{aligned}
&\min_{\rho} && \max \quad (-u^{e}_{\text{out}}),(-u^{i}_{\text{out}}),(-u^{d}_{\text{out}}), && \text{(5.3a)}\\
&\text{Subject to} && \mathbf{K}(\boldsymbol{\rho}^{\text{e}})\mathbf{U}^{\text{e}} = \mathbf{F}^{\text{e}}, && \text{(5.3b)}\\
& && \mathbf{K}(\boldsymbol{\rho}^{\text{i}})\mathbf{U}^{\text{i}} = \mathbf{F}^{\text{i}}, && \text{(5.3c)}\\
& && \mathbf{K}(\boldsymbol{\rho}^{\text{d}})\mathbf{U}^{\text{d}} = \mathbf{F}^{\text{d}}, && \text{(5.3d)}\\
& && \frac{V(\boldsymbol{\rho}^{i})}{V_0} - f_0 \leq 0, && \text{(5.3e)}\\
& && \left[\frac{1}{n}\sum_{i=1}^{n} g_i^{P}\right]^{\frac{1}{P}} - 1 \leq 0, && \text{(5.3f)}\\
& && \mathbf{G}^{(J)}\mathbf{T}^{(J)} = \mathbf{Q}^{(J)}, && \text{(5.3g)}\\
& && 0 \leq \rho \leq 1, && \text{(5.3h)}
\end{aligned}$$

where u^{e}_{out}, u^{i}_{out} and u^{d}_{out} are the output displacements at the output port for the eroded, intermediate and dilated design. $\boldsymbol{\rho}^{\text{e}}$, $\boldsymbol{\rho}^{\text{i}}$ and $\boldsymbol{\rho}^{\text{d}}$ are the densities of the eroded, intermediate and dilated design. Changes were made to the MATLAB code to incorporate the robust formulation; the results will be shown in the following section.

5.6. Influence of robust formulation

The robust method has multiple parameters which can be altered to change the behaviour of the method. Two of the most important parameters are the threshold value η and β multiplication factor. Increasing the β multiplication value will tighten the optimization process, which means the amount of material which can change location per iteration will decrease quicker. The chosen threshold value η was 0.3 and a multiplication factor of 1.3, which was applied every 50 iterations until the maximum β_{max} of 70 was reached, was used. The optimization is stopped when both the volume and if used, the hotspot constraint is met.

5.6.1. Parameters used

The first optimization was performed without the hotspot constraint and it was noticed that the optimization process could not find a solution to the robust problem. The volume constraint was not satisfied and eroded design disconnected, which led to an objective value of zero. Multiple changes were made to get the optimization process to work as intended. The Method of Moving Asymptotes (MMA) is used to solve the problem. One can tune the MMA process by changing some of the coefficients. One of those coefficients is the c_i value, it ensures that the constraint is expensive for the optimization process compared to the objective, so that the constraint is not violated [25]. As the optimization process is not successful for these values, the c_i value was tweaked. A commonly used value for c_i, is 1000. After multiple tests, it was concluded that a higher value resulted in an even worse result. Lowering the value had a positive effect on the outcome. For a value of 100, the process was close to working. Using a value of 50 for the c_i proved to work the best. Next to that, it was found out that increasing the volume fraction to 0.4 resulted in a working optimization process as there was enough material for the optimizer to use. Therefore, from this point onwards, a volume fraction V_f of 0.4 will be used. Some of the failed attempts listed above can be found in the appendix at the end of this thesis.

5.6.2. Without hotspot constraint

An optimization without the hotspot constraint was done to set a benchmark to be able to see the influence of introducing a hotspot constraint to the optimization problem. The same boundary conditions as in Sec. 3.2 are used and the printed orientation is used. The parameters used can be seen in Tab. 5.3, where the notable changes from previous optimizations are the volume fraction f_0 of 0.4 and the thermal penalty r of 3. The obtained eroded, intermediate and dilated designs can be seen in Fig. 5.8. The robust method has improved the M_{nd} value by a large amount as it is now only 1.1%, which is significantly lower than the 30–40 % M_{nd} values obtained without using the robust method. The objective value of all three designs per iteration can be seen in Fig. 5.9, with in the end an objective value $u_{\text{out}} = 35.5$ for the intermediate design. The number of iterations is more than doubled due to the robust formulation. It can be noticed that the objective value for

Table 5.3: Constant parameters used in the robust optimization

Parameter	Value
E_0	1
E_{min}	$10^{-}6$
nelx	160
nely	80
p	3
r_{min}	6
f_0	0.4

the eroded design is much lower than for the intermediate and dilated design. This is due to the extremely thin member located near the bottom of the design, indicated by the red arrow. This might also be the reason why the fluctuations in the objective of the eroded design are stronger compared to the other two designs. The objective value for the same case and parameters without the robust method was obtained in Sect. 3.5, where the objective value for a volume fraction of 0.4 was 35.6. Which means for this case, the introduction of the robust method had a positive effect.

Figure 5.8: Resulting eroded (left), intermediate (middle) and dilated (right) topologies from robust CM TO without hotspot constraint with an output displacement for the intermediate design $u_{\text{out}} = 35.5$. The red arrow indicates a very thin member of the eroded design

The intermediate design was analysed using the hotspot method [17]. The resulting temperature field can be seen in Fig. 5.10, where the maximum relative temperature is 6.19. This hotspot analysis was done to set a benchmark maximum temperature before the hotspot constraint is used. In the next section, the hotspot constraint will be included in the optimization process.

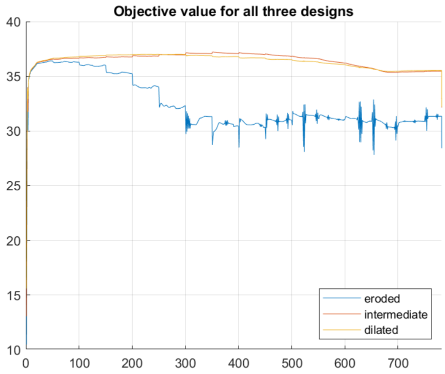

Figure 5.9: Objective values for the eroded, intermediate and dilated designs for every iteration

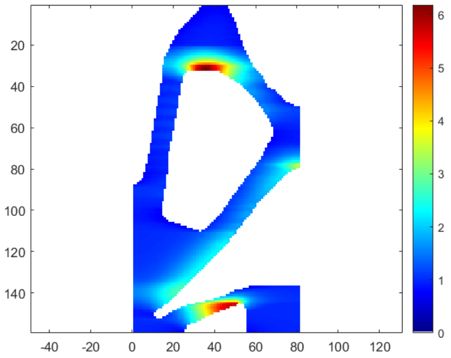

Figure 5.10: Temperature field for the design obtained with a robust method, with a maximum normalized temperature of 6.19

5.6.3. With hotspot constraint

In this section, the hotspot constraint is added to the robust optimization method for compliant mechanisms. The hotspot constraint was applied on the intermediate design as that is the end product of the optimization. The hotspot penalty value r is 3, the slab thickness s is 12 and the printed orientation is used. All the parameters can be seen in Tab. 5.3. The critical temperature used was not the same as in all the other optimizations, this is the case because it was observed that the optimizer already had trouble solving the robust case without the hotspot constraint. Therefore, a critical temperature $T_{\text{crit}} = 3.04$ was used. The obtained eroded, intermediate and dilated designs can be seen in Fig. 5.11, where the objective value for the intermediate design $u_{\text{out}} = 35.2$. The objective value is only reduced by 0.3, which is a relatively small difference. It can be observed that the addition of the hotspot constraint has resulted in the addition of a pillar at the bottom of the design which can be used to transport heat from the flexure right on top of it, which is pointed out by the red arrow. The objective value for all three cases per iteration can be seen in Fig. 5.12, it is again noticed that the eroded design has a much lower objective value than the other two cases. A possible reason for this is that the eroded design is close to disconnecting as can be seen in the left design in Fig. 5.11. Both the constraint values per iteration can be seen in Fig. 5.13, where it can be observed that the hotspot constraint is quickly satisfied and the volume constraint takes a lot more time to satisfy. This figure was mainly included to show how the constraint plot looks when the optimization is successful, as later figures will show dissatisfied constraints. Fig. 5.14 shows the temperature field of the obtained design, with a maximum normalized temperature $T_{\text{crit}} = 3.04$. The location of the maximum temperatures is similar to the design obtained without the hotspot constraint, areas with a large overhang angle. However, the maximum temperature is successfully reduced by more than 50 % due to the hotspot constraint. The percentage of grey area, $M_{\text{nd}} = 2.66\%$, which is a very good result as it is significantly lower than the 30–40 % achieved without the robust method. A lower M_{nd} percentage means that the threshold used in post-processing will have a much smaller effect than with the printed design. The next section will evaluate a different print orientation.

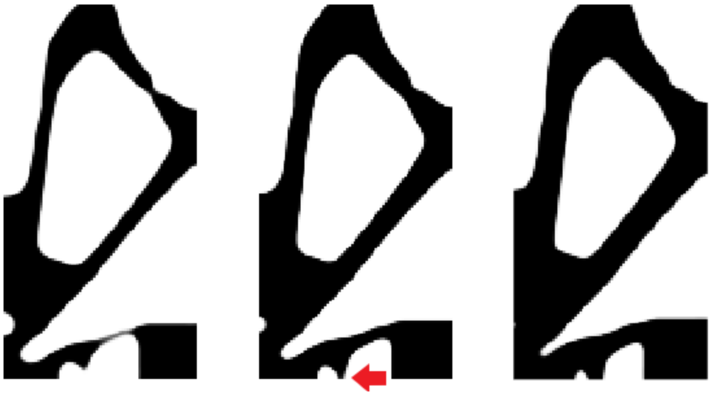

Figure 5.11: Resulting eroded (left), intermediate (middle) and dilated (right) topologies from robust CM TO with hotspot constraint with an output displacement for the intermediate design $u_{\text{out}} = 35.2$. The red arrow indicates a pillar which was added as a result of adding the hotspot constraint

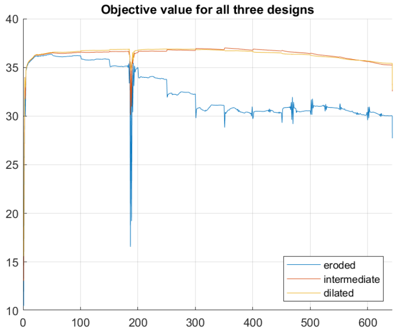

Figure 5.12: Objective values of the eroded, intermediate and dilated designs per iteration

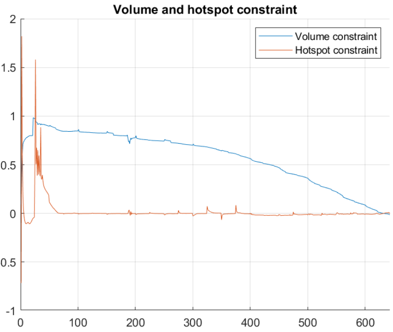

Figure 5.13: Volume and hotspot constraint values per iteration

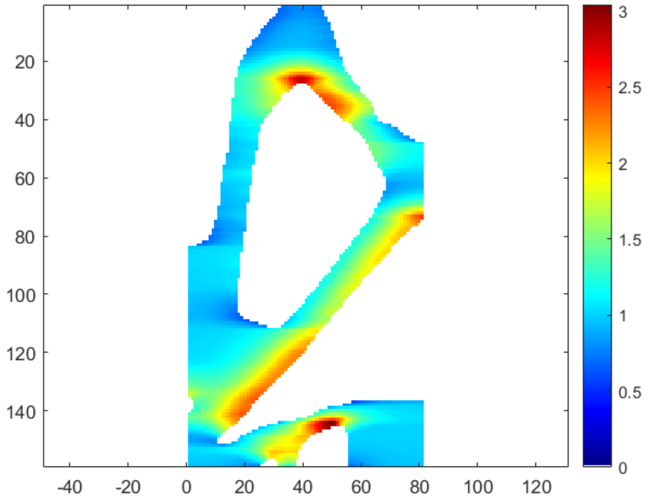

Figure 5.14: Temperature field for the design obtained with robust CM TO with hotspot constraint, with a maximum relative temperature $T_{\text{crit}} = 3.04$

5.6.4. West orientation

In this section the same boundary conditions and parameters are used as in the section above, but the print orientation in the hotspot constraint was changed to see if the optimizer could find a solution to this different problem. The base plate was located at the west of the design for this optimization. The resulting eroded, intermediate and dilated designs can be seen in Fig. 5.15, with an objective value u_{out} = 34.9 for the intermediate design. This is almost similar to the objective value of the printed orientation and the case without the hotspot constraint. The percentage of grey area, M_{nd} = 0.79%, which is again a very good result and a sign that the robust method works as intended. Compared to the printed orientation, this design has a member which looks like a flexure. The objective values for the three cases per iteration can be seen in Fig. 5.16, where it can be noticed that the eroded version has a much smaller objective value than the other two designs similar to the printed orientation. It can also be seen that the optimization was stopped at 1200 iterations, this was the case as the optimization was not converging as can be seen in the constraints plot. Fig. 5.17

Figure 5.15: Resulting eroded (left), intermediate (middle) and dilated (right) topologies from robust CM TO with hotspot constraint with the base plate on the west side of the design, with an output displacement for the intermediate design u_{out} = 34.9

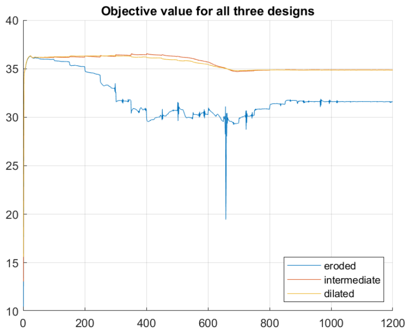

Figure 5.16: Objective values of the eroded, intermediate and dilated designs per iteration

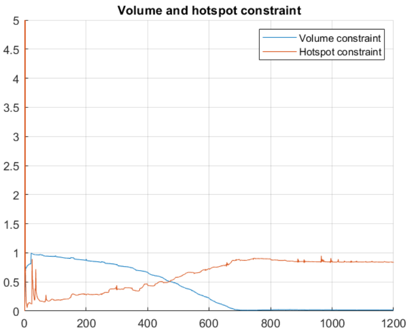

Figure 5.17: Volume and hotspot constraint values per iteration

shows the constraint values per iteration and it can be seen that the hotspot constraint is not met. Where the volume constraint is satisfied after about 700 iterations, the hotspot constraint continues to rise. This means the optimizer is not able to find a solution to the problem. Looking at the temperature field might give insight into why the hotspot constraint is not satisfied. The temperature field can be seen in Fig. 5.18b and the temperature field of the robust design without hotspot constraint analysed with the base plate on the west side can be seen in Fig. 5.10. The addition of the hotspot constraint has had a large impact on the maximum temperature. the large overhang in the design obtained without the hotspot constraint has been reduced so that the temperature achieved is also much lower. It can also be noticed that the main problem, which the optimizer cannot solve, is the block of material located at the bottom of the design. This block was artificially added to the design so that there was a part of the design which could be clamped. Due to the lower maximum temperature, less support material might have to be placed to print the gripper.

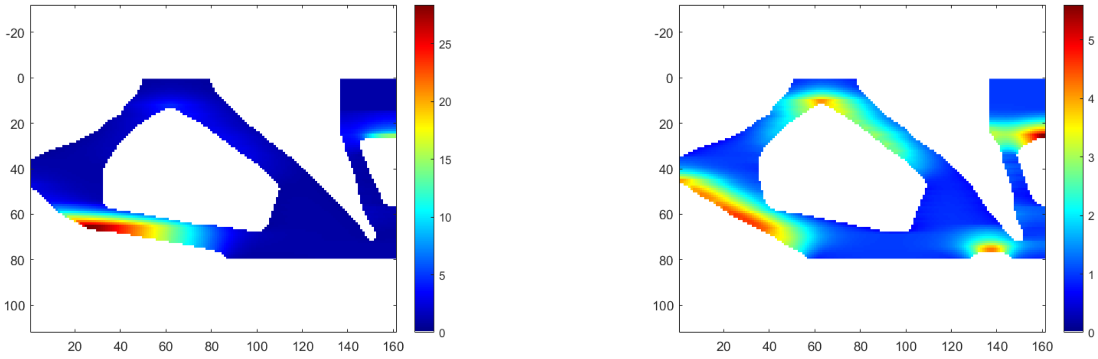

(a) Temperature field for the design obtained with robust CM TO without hotspot constraint and the base plate on the west side of the design, with a maximum relative temperature $T_{\mathrm{crit}} = 28.38$

(b) Temperature field for the design obtained with robust CM TO with hotspot constraint and the base plate on the west side of the design, with a maximum relative temperature $T_{\mathrm{crit}} = 5.60$

Figure 5.18: Temperature field analysed with the base plate on the west side of the designs

5.6.5. East orientation

In this section, the base plate is located at the east side of the designs. This case proved to be the most difficult for the optimizer to solve, which is why it was chosen. The same boundary conditions and parameters are used as in the sections above. The resulting obtained eroded, intermediate and dilated designs can be seen in Fig. 5.19, where the output displacement of the intermediate design $u_{\mathrm{out}} = 34.7$. This is similar to the results mentioned above. For the eroded and intermediate design, material is removed inside the gripper at the top, whereas that is not the case for the dilated design. This might be the case because there is too much material used and removing material at that position has the least negative influence on the design. It can also be noticed that the flexure attached to the block is nearly disconnected in the eroded design. The percentage of greyness $M_{\mathrm{nd}} = 0.74\%$, which is a good result. The objective values of the eroded, intermediate

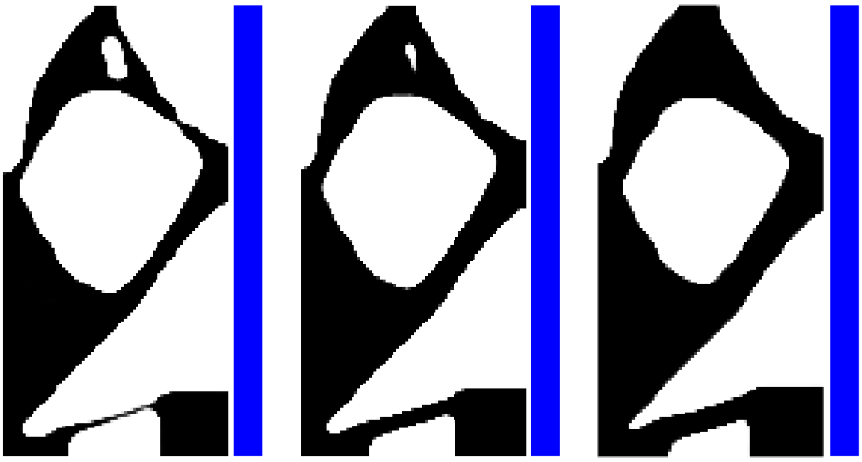

Figure 5.19: Resulting eroded (left), intermediate (middle) and dilated (right) topologies from robust CM TO with hotspot constraint with the base plate on the east side of the design, with an output displacement for the intermediate design $u_{\text{out}} = 34.7$

and dilated designs per iteration can be seen in Fig. 5.20, where it can be seen that also for this orientation, the eroded design has a much lower objective value than the other two designs. This appears to be a problem for all orientations. Both the constraint values can be seen in Fig. 5.21. As can be seen, both constraints are not satisfied. The volume constraint value is very close to zero, but the hotspot constraint is nowhere near sufficient. This was also the case in the previous section, where the base plate was located on the west side of the designs. Both situations gave a similar constraints plot, where the volume constraint is slowly decreasing and the hotspot constraint increases per iteration until it reaches a certain point where the design barely changes. Fig. 5.22a shows the temperature field of the design obtained without the hotspot constraint, analysed with the base plate on the east side of the design and Fig. 5.22b shows the temperature field of the design obtained in this section. The maximum temperature is drastically reduced, by more than a factor 6. Again, the critical areas of the obtained design are the areas with a large overhanging part.

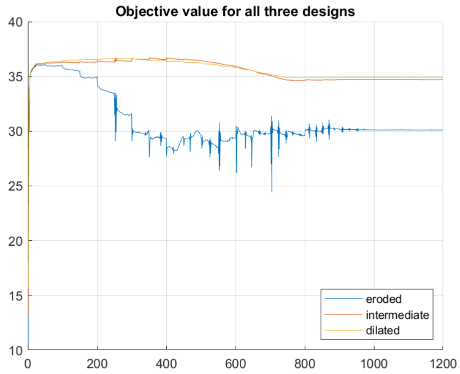

Figure 5.20: Objective values of the eroded, intermediate and dilated designs per iteration

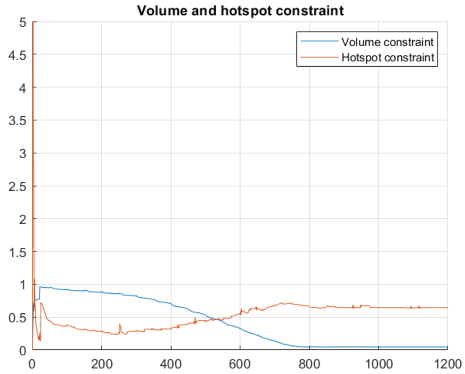

Figure 5.21: Volume and hotspot constraint values per iteration

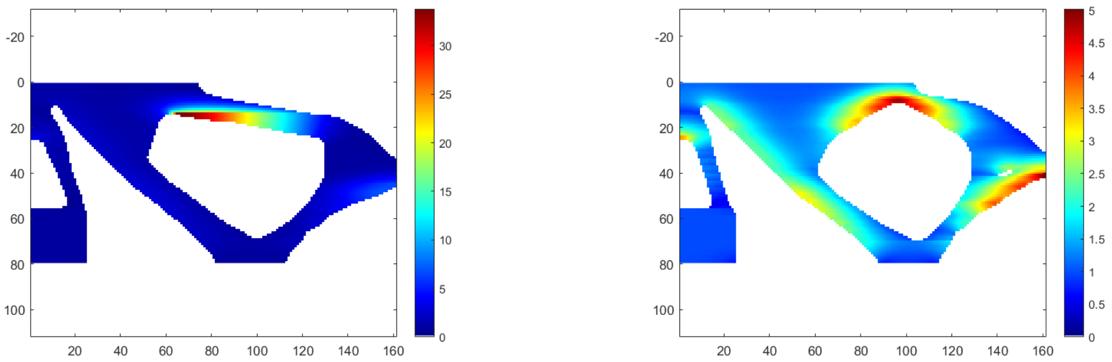

(a) Temperature field for the design obtained with robust CM TO and the base plate on the east side of the design, with a maximum relative temperature $T_{\mathrm{crit}} = 33.78$

(b) Temperature field for the design obtained with robust CM TO with hotspot constraint and the base plate on the east side of the design, with a maximum relative temperature $T_{\mathrm{crit}} = 5.60$

Figure 5.22: Temperature field analysed with the base plate on the east side of the designs

5.6.6. Different slab thickness

In this section, the slab thickness is changed to see what kind of influence it has on the resulting design and temperature field. In the sections above, a slab thickness $s = 12$ was used. In this section a slab thickness $s = 24$ will be used. The printed orientation will be used and the two different slab thicknesses will be compared. The resulting three designs from the robust method can be seen in Fig. 5.23, with an output displacement $u_{\mathrm{out}} = 35.3$ for the intermediate design. This is a little bit higher than the resulting displacement for the case where a slab thickness of 12 was used, where the displacement was 35.2. The designs are extremely similar. The same goes for the objectives and constraints plot, which is why they are not shown here. The temperature field however does differ, as can be seen in Figs. 5.24a and 5.24b, where the temperature fields of both slab thicknesses are displayed. The locations of the maximum temperatures are still the same, but the area of these high temperatures is much larger when using a larger slab thickness. For a slab thickness of 12, the maximum temperatures are located at specific small parts of the design.

Figure 5.23: Resulting eroded (left), intermediate (middle) and dilated (right) topologies from robust CM TO with hotspot constraint with the base plate on the south side of the design and using a slab thickness $s = 24$, with an output displacement for the intermediate design $u_{\mathrm{out}} = 35.3$

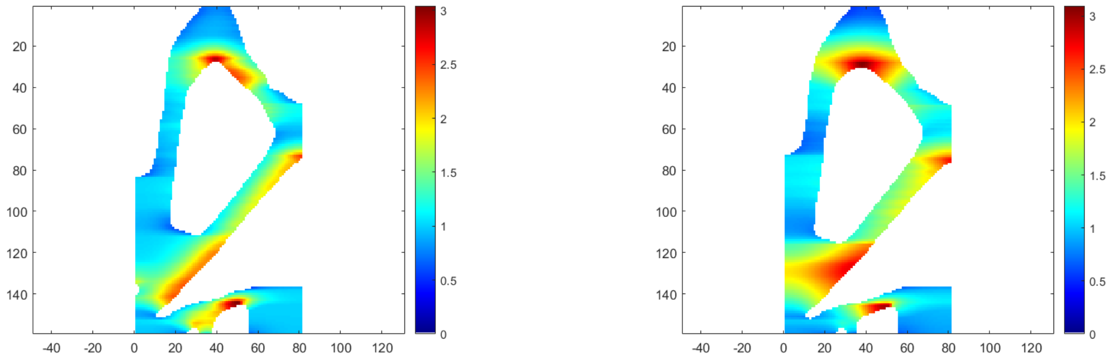

(a) Temperature field for the design obtained with robust CM TO with hotspot constraint and the base plate on the south side of the design and a slab thickness $s = 12$, with a maximum relative temperature $T_{\text{crit}} = 3.04$

(b) Temperature field for the design obtained with robust CM TO with hotspot constraint and the base plate on the south side of the design and a slab thickness $s = 24$, with a maximum relative temperature $T_{\text{crit}} = 3.09$

Figure 5.24: Temperature field analysed with the base plate on the south side of the designs

5.7. Concluding remarks

In this chapter, the hotspot constraint was added to the optimization process and its effect was evaluated. The first trials showed promising results but had a major problem with the high percentage of intermediate density. This problem could partially be solved by reducing the filter radius, but that only worked for the printed orientation and not for any other orientation. Following these findings, the robust design method was introduced. This method was able to reduce the percentage of intermediate density by a large amount, but it also had negative effects. The optimization problem became much more complex and needed a lot of tweaking to find the right parameters to get a successful working optimization process. When the right parameters were chosen, the optimizer was able to reduce the maximum temperature by a large amount while maintaining a relatively high objective value. It was however not successful in completely satisfying the constraint for other orientations than the printed orientation. In conclusion, it can be said that the addition of the hotspot constraint can have a positive effect on the design as the maximum temperature is lowered which can have an influence on the amount of support material needed for printing. However precise control of temperatures and volume proves difficult, the optimization process becomes more parameter-dependent and the number of required iterations is increased considerably.

6

Conclusions and recommendations

6.1. Conclusions

In this thesis, a CM was designed using TO and printed using AM. The design was analysed using a physical experiment and multiple simulations. Also, a hotspot constraint was added to a TO code for compliant mechanisms, the constraint performance was evaluated and a robust method was used for improving TO efficacy. The aims of this thesis were twofold:

1. To determine the extent of overheating defects in metal printed CMs generated by conventional TO
2. To determine the effectiveness of reducing overheating in TO-generated CMs by adding an overheating constraint in the TO process

To study the first point, a gripper was designed and printed in Inconel 625. After printing, multiple sizes of the gripper were evaluated using a force/displacement test and using a simulation of the physical experiment. It was noticed that the results were not similar, it can be concluded that printing a CM design does not necessarily guarantee similar behaviour between the model and the printed design. It can also be concluded that certain thresholds used in conventional topology optimization to obtain a printable design have a large influence on the resulting behaviour of a design. Also, for small designs, support material can make designs useless if the support material cannot be safely removed. No overheating defects were observed in the printed designs by visual inspection, however literature shows overheating during printing can be a problem and the resulting defects are not always visible.

This leads to the second aim, which was studied by introducing a hotspot constraint to the TO formulation used to design the printed gripper. Multiple parameters were evaluated and it was concluded that the constraint had a positive effect, i.e. it could reduce the maximum temperature while maintaining a relatively high objective value. However, the percentage of intermediate densities in the designs was near 30%. As a threshold needs to be applied before a design can be printed, this high value will result in a bad representation of what will really be printed.

The capability of the robust method has been studied to reduce this problem. This approach proved quite sensitive to parameter choices. After tuning multiple parameters, the optimizer was able to generate a design with a very low percentage of intermediate densities while satisfying both the volume and hotspot constraint. It was however too difficult for the optimizer to reduce the temperature to a level as low as Ranjan et al. [17] were able to do. One of the problems was that the eroded design was disconnecting for certain parameters, thus for each different orientation used a process of finding suitable parameters was needed before a successful design could be obtained. It could be concluded that the optimization problem was very difficult due to contradicting objectives. Where the hotspot constraint needs more material at a location to be satisfied, the objective needs less material to be as high as possible. The addition of the hotspot constraint reduced the overheating during printing and reduces the need of support material during printing.

This thesis contributes to the research fields of CMs, TO and metal additive manufacturing. It has contributed to the understanding of the hotspot constraint and the influence it has on the generation of CMs. This research can help future engineers who are interested in printing metal CMs.

6.2. Recommendations

In this section, relevant recommendations for future research of TO of metal compliant mechanisms are listed.

6.2.1. Design generation using TO and additive manufacturing

- During the process of defining the problem that the optimizer needs to solve, the physical experiment which will be done after the design is printed, should be considered so that any test setup that needs to be build or printed can be made beforehand. This is expected to improve the similarity between simulation and measurement results.

- Doing a finite element analysis of the experiment before the gripper is printed can give valuable insight in the amount of force needed to move the gripper. This information can then be used to look for a suitable test location.

- The percentage of intermediate densities in the design should be considered before printing as the design might change significantly after applying a threshold. Using a robust optimization method is recommended, as it was found to solve the issue of intermediate densities.

- The printing process and removal from the base plate should be considered before the final design is to be printed, in this thesis that would have resulted in a useful gripper of the smallest size.

6.2.2. Experiments and simulations

- Proper STL files should be obtained either by changing the process of acquiring them or repairing the files, to do a simulation which is an exact copy of the physical experiment.

- Printing the design in plastic and testing it would give insight into how the metal design might react to forces. This information will help decide the specifications of the printed design before printing.

- Printing and testing of the design obtained from the topology optimization with hotspot constraint can give insight into the effect of the hotspot constraint.

6.2.3. Hotspot constraint

- More research must be done on the various parameters available and the effect of each of them (e.g. the critical temperature T_{crit}, the beta multiplication factor and the threshold value η), as at this moment it is not clear what values for each parameter work the best. This is an important step to achieve meeting the hotspot constraint for all designs.

- A 3D version of the TO process should be developed to make full use of the 3D design freedom and directly obtain printable grippers, instead of attaching multiple parts as done in this thesis.

- The effect of the hotspot constraint on the amount of support material needed, should be studied, so that the use can be validated and in future designs, the hotspot constraint can reduce the amount of support material needed.

Bibliography

[1] Erik Andreassen, Anders Clausen, Mattias Schevenels, Boyan Lazarov, and Ole Sigmund. Efficient topology optimization in matlab using 88 lines of code. *Structural and Multidisciplinary Optimization*, 43: 1–16, 11 2011. doi: 10.1007/s00158-010-0594-7.

[2] M. Bendsøe and O. Sigmund. *Topology optimization. Theory, methods, and applications. 2nd ed., corrected printing.* 01 2004. doi: 10.1007/978-3-662-05086-6.

[3] M. P. Bendsøe and N. Kikuchi. Generating optimal topologies in structural design using a homogenization method. *Computer Methods in Applied Mechanics and Engineering*, 71(2):197 – 224, 1988. ISSN 0045-7825. doi: https://doi.org/10.1016/0045-7825(88)90086-2. URL `http://www.sciencedirect.com/science/article/pii/0045782588900862`.

[4] Martin P Bendsøe and Ole Sigmund. Material interpolation schemes in topology optimization. *Archive of applied mechanics*, 69(9-10):635–654, 1999.

[5] T. E. Bruns and D. A. Tortorelli. Topology optimization of non-linear elastic structures and compliant mechanisms. *Computer Methods in Applied Mechanics and Engineering*, 190(26):3443 – 3459, 2001. ISSN 0045-7825. doi: https://doi.org/10.1016/S0045-7825(00)00278-4. URL `http://www.sciencedirect.com/science/article/pii/S0045782500002784`.

[6] L. Cao, A. Dolovich, and W. J. Zhang. On understanding of design problem formulation for compliant mechanisms through topology optimization. *Mechanical Sciences*, 4(2):357–369, 2013. doi: 10.5194/ms-4-357-2013. URL `https://www.mech-sci.net/4/357/2013/`.

[7] Robert D. Cook, David S. Malkus, Michael E. Plesha, and Robert J. Witt. *Concepts and applications of finite element analysis.* Wiley, 2001.

[8] Tom Craeghs, Florian Bechmann, Sebastian Berumen, and Jean-Pierre Kruth. Feedback control of layerwise laser melting using optical sensors. *Physics Procedia*, 5:505–514, 2010.

[9] W. E. Frazier. Metal additive manufacturing: A review. *Journal of Materials Engineering and Performance*, 23(6):1917–1928, Jun 2014. ISSN 1544-1024. doi: 10.1007/s11665-014-0958-z. URL `https://doi.org/10.1007/s11665-014-0958-z`.

[10] Jivtesh Khurana, Bradley Hanks, and Mary Frecker. Design for Additive Manufacturing of Cellular Compliant Mechanism Using Thermal History Feedback. Volume 2A: 44th Design Automation Conference, 08 2018. doi: 10.1115/DETC2018-85819. URL `https://doi.org/10.1115/DETC2018-85819`. V02AT03A035.

[11] Lionel Kiener, Herve Saudan, Florent Cosandier, Johan Kruis, Gérald Perruchoud, Václav Pejchal, Peter Spanoudakis, and Julien Rouvinet. Innovative concept for additive manufacturing of compliant mechanisms. 09 2019.

[12] M. Leary, M. McMillan, D. Shidid, H. VanToor, M. Mazur, and M. Brandt. Numerical methods to predict overheating in slm lattice structures. *International Congress on Applications of Lasers & Electro-Optics*, 2014(1):895–902, 2014. doi: 10.2351/1.5063139. URL `https://lia.scitation.org/doi/abs/10.2351/1.5063139`.

[13] J. Liu, A. T. Gaynor, S. Chen, Z. Kang, K. Suresh, A. Takezawa, L. Li, J. Kato, J. Tang, C. C. L. Wang, L. Cheng, X. Liang, and A. C. To. Current and future trends in topology optimization for additive manufacturing. *Structural and Multidisciplinary Optimization*, 57(6):2457–2483, Jun 2018. ISSN 1615-1488. doi: 10.1007/s00158-018-1994-3. URL `https://doi.org/10.1007/s00158-018-1994-3`.

[14] R. Mertens, S. Clijsters, K. Kempen, and J.-P. Kruth. Optimization of scan strategies in selective laser melting of aluminum parts with downfacing areas. *Journal of Manufacturing Science and Engineering*, 136, 12 2014. doi: 10.1115/1.4028620.

[15] A. Midha, T. W. Norton, and L. L. Howell. On the Nomenclature, Classification, and Abstractions of Compliant Mechanisms. *Journal of Mechanical Design*, 116(1):270–279, 03 1994. ISSN 1050-0472. doi: 10.1115/1.2919358. URL `https://doi.org/10.1115/1.2919358`.

[16] L.A. Parry, I.A. Ashcroft, and R.D. Wildman. Geometrical effects on residual stress in selective laser melting. *Additive Manufacturing*, 25:166 – 175, 2019. ISSN 2214-8604. doi: https://doi.org/10.1016/j.addma.2018.09.026. URL `http://www.sciencedirect.com/science/article/pii/S2214860418304202`.

[17] R. Ranjan, Y. Yang, C. Ayas, M. Langelaar, and F. van Keulen. Local overheating prevention in topology optimization for additive manufacturing.

[18] Rajit Ranjan, Can Ayas, Matthijs Langelaar, and Fred van Keulen. Fast detection of heat accumulation in powder bed fusion using computationally efficient thermal models. *Materials*, 13(20):4576, Oct 2020. ISSN 1996-1944. doi: 10.3390/ma13204576. URL `http://dx.doi.org/10.3390/ma13204576`.

[19] W. J. Sames, F. A. List, S. Pannala, R. R. Dehoff, and S. S. Babu. The metallurgy and processing science of metal additive manufacturing. *International Materials Reviews*, 61(5):315–360, 2016. doi: 10.1080/09506608.2015.1116649. URL `https://doi.org/10.1080/09506608.2015.1116649`.

[20] O. Sigmund. A 99 line topology optimization code written in matlab. *Structural and Multidisciplinary Optimization*, 21(2):120–127, 2001. ISSN 1615147X. doi: 10.1007/s001580050176.

[21] O. Sigmund. Morphology-based black and white filters for topology optimization. *Structural and Multidisciplinary Optimization*, 33(4):401–424, Apr 2007. ISSN 1615-1488. doi: 10.1007/s00158-006-0087-x. URL `https://doi.org/10.1007/s00158-006-0087-x`.

[22] O. Sigmund and K. Maute. Topology optimization approaches. *Structural and Multidisciplinary Optimization*, 48(6):1031–1055, Dec 2013. ISSN 1615-1488. doi: 10.1007/s00158-013-0978-6. URL `https://doi.org/10.1007/s00158-013-0978-6`.

[23] Ole Sigmund and M Bendsoe. Topology optimization. *State-of-the-Art and Future Perspectives, Copenhagen: Technical University of Denmark (DTU)*, 2003.

[24] Krister Svanberg. The method of moving asymptotes—a new method for structural optimization. *International Journal for Numerical Methods in Engineering*, 24(2):359–373, 1987. doi: 10.1002/nme.1620240207. URL `https://onlinelibrary.wiley.com/doi/abs/10.1002/nme.1620240207`.

[25] Krister Svanberg. The method of moving asymptotes-modelling aspects and solution schemes. *Lecture Notes for the DCAMM course Advanced Topics in Structural Optimization*, 1998.

[26] Ming Tang, P. Chris Pistorius, and Jack L. Beuth. Prediction of lack-of-fusion porosity for powder bed fusion. *Additive Manufacturing*, 14:39–48, 2017. ISSN 2214-8604. doi: https://doi.org/10.1016/j.addma.2016.12.001. URL `https://www.sciencedirect.com/science/article/pii/S2214860416300471`.

[27] Fengwen Wang, Boyan Stefanov Lazarov, and Ole Sigmund. On projection methods, convergence and robust formulations in topology optimization. *Structural and Multidisciplinary Optimization*, 43(6):767–784, 2011.

[28] Tomás Zegard and Glaucio H Paulino. Bridging topology optimization and additive manufacturing. *Structural and Multidisciplinary Optimization*, 53(1):175–192, 2016.

[29] Xianmin Zhang and Benliang Zhu. *Topology optimization of compliant mechanisms*. Springer, 2018.

[30] B. Zhu, X. Zhang, H. Zhang, J. Liang, H. Zang, H. Li, and R. Wang. Design of compliant mechanisms using continuum topology optimization: A review. *Mechanism and Machine Theory*, 143:103622, 2020. ISSN 0094-114X. doi: https://doi.org/10.1016/j.mechmachtheory.2019.103622. URL `http://www.sciencedirect.com/science/article/pii/S0094114X19315538`.

A

Appendix: Sensitivity Analysis of the hotspot constraint

This appendix explains the sensitivity derivation, which comes straight out of the paper by Ranjan et al. [17]. The sensitivity of the thermal constraint with respect to design variable ρ is derived using the adjoint method. The augmented constraint is written as follows,

$$f^* = f + \sum_{J=1}^{m} (\boldsymbol{\lambda}^{(J)})^T (\mathbf{Q}^{(J)} - \mathbf{G}^{(J)}\mathbf{T}^{(J)}), \tag{A.1}$$

with $\boldsymbol{\lambda}^{(J)}$ as the Lagrange multiplier vector for the Jth slab. Differentiating the augmented constraint with respect to element density $\tilde{\rho}_e$ gives

$$\frac{\partial f^*}{\partial \tilde{\rho}_e} = \frac{\partial f}{\partial \tilde{\rho}_e} + \sum_{J=1}^{m} (\boldsymbol{\lambda}^{(J)})^T \left(\frac{\partial \mathbf{Q}^{(J)}}{\partial \tilde{\rho}_e} - \mathbf{G}^{(J)} \frac{\partial \mathbf{T}^{(J)}}{\partial \tilde{\rho}_e} - \frac{\partial \mathbf{G}^{(J)}}{\partial \tilde{\rho}_e} \mathbf{T}^{(J)} \right). \tag{A.2}$$

Expansion of the first term in the RHS of Eq. (A.2) gives

$$\frac{\partial f}{\partial \tilde{\rho}_e} = \frac{\left[\frac{1}{n} \sum_{i=1}^{n} (g_i^P) \right]^{(\frac{1}{P})-1}}{n (T^{\mathrm{cr}})^P N_c} \left[(\tilde{\mathbf{T}}^{\Omega_D})^{P-1} \right]^T \sum_{J=1}^{m} \mathbf{L}^{(J)} \frac{\partial \mathbf{T}^{(J)}}{\partial \tilde{\rho}_e}. \tag{A.3}$$

In order to avoid computation of state sensitivities, all the terms with $\partial \mathbf{T}^{(J)} / \partial \tilde{\rho}_e$ are combined. This leads to the following sensitivity expression:

$$\frac{\partial f^*}{\partial \tilde{\rho}_e} = \sum_{J=1}^{m} \left(\boldsymbol{\lambda}^{(J)} \right)^T \left(\frac{\partial \mathbf{Q}^{(J)}}{\partial \tilde{\rho}_e} - \frac{\partial \mathbf{G}^{(J)}}{\partial \tilde{\rho}_e} \mathbf{T}^{(J)} \right). \tag{A.4}$$

Here, $\boldsymbol{\lambda}^{(J)}$ is the solution of following,

$$\frac{\left[\frac{1}{n} \sum_{i=1}^{n} (g_i^P) \right]^{(\frac{1}{P}-1)}}{n (T^{\mathrm{cr}})^P N_c} \left[(\tilde{\mathbf{T}}^{\Omega_D})^{P-1} \right]^T \boldsymbol{M}\mathbf{L}^{(J)} - (\boldsymbol{\lambda}^{(J)})^T \mathbf{G}^{(J)} = 0, \tag{A.5}$$

where $J = 1, \ldots, m$. Furthermore, expressions for $\partial \mathbf{G}^{(J)} / \partial \tilde{\rho}_e$ and $\partial \mathbf{Q}^{(J)} / \partial \tilde{\rho}_e$ can be found by differentiating Eq. 2.17 and Eq. 2.18, respectively. Sensitivities with respect to the design variables are calculated using the following chain rule,

$$\frac{\partial f^*}{\partial \rho_e} = \frac{\partial f^*}{\partial \tilde{\rho}_e} \frac{\partial \tilde{\rho}_e}{\partial \rho_e}. \tag{A.6}$$

B

Extra TO with hotspot constraint results for various filter radii

This appendix consists of results from the robust topology optimization (TO) with hotspot constraint. The following results were obtained using a critical temperature of 2, a volume fraction of 0.4 and a β multiplication factor of 1.2.

B.1. Filter radius $r_{\text{min}} = 3$

Figure B.1: Resulting eroded (left), intermediate (middle) and dilated (right) topologies from robust CM TO with hotspot constraint with an output displacement for the intermediate design $u_{\text{out}} = 35.8$.

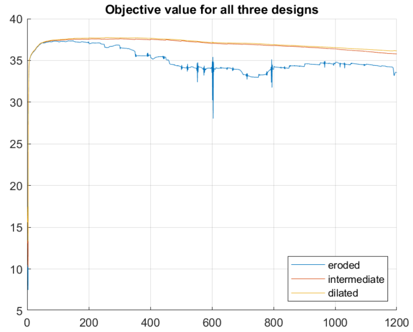

Figure B.2: Objective values of the eroded, intermediate and dilated designs per iteration

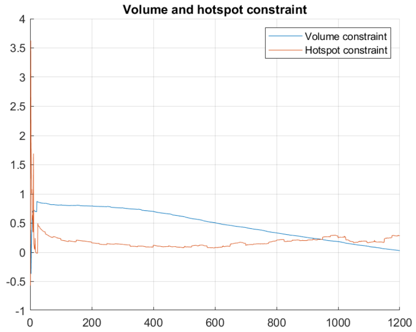

Figure B.3: Volume and hotspot constraint values per iteration

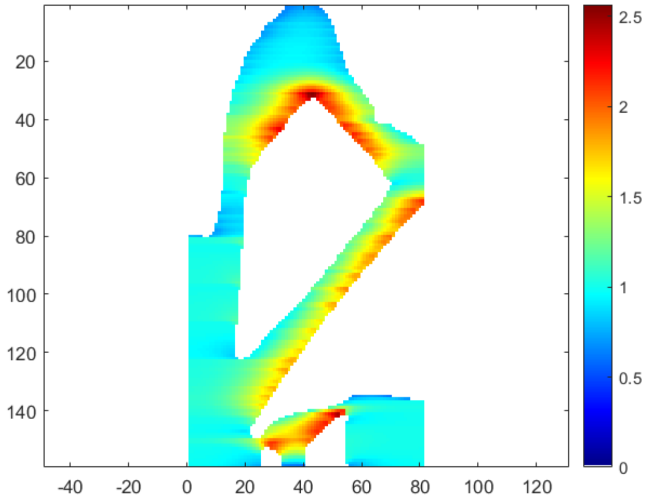

Figure B.4: Temperature field for the design obtained with robust CM TO with hotspot constraint, with a maximum relative temperature $T_{\text{crit}} = 2.56$

B.2. Filter radius $r_{\text{min}} = 6$

Figure B.5: Resulting eroded (left), intermediate (middle) and dilated (right) topologies from robust CM TO with hotspot constraint with an output displacement for the intermediate design $u_{\text{out}} = 34.6$.

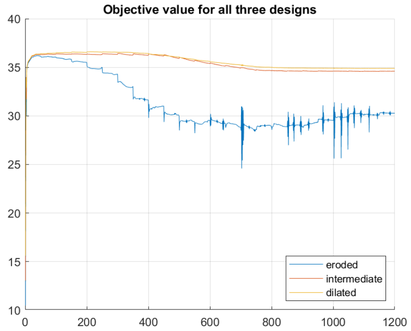

Figure B.6: Objective values of the eroded, intermediate and dilated designs per iteration

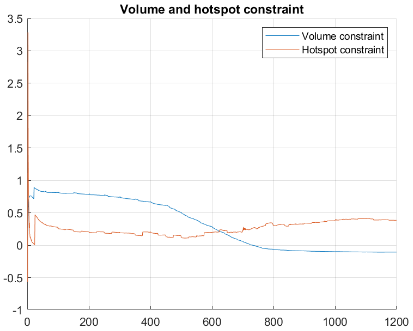

Figure B.7: Volume and hotspot constraint values per iteration

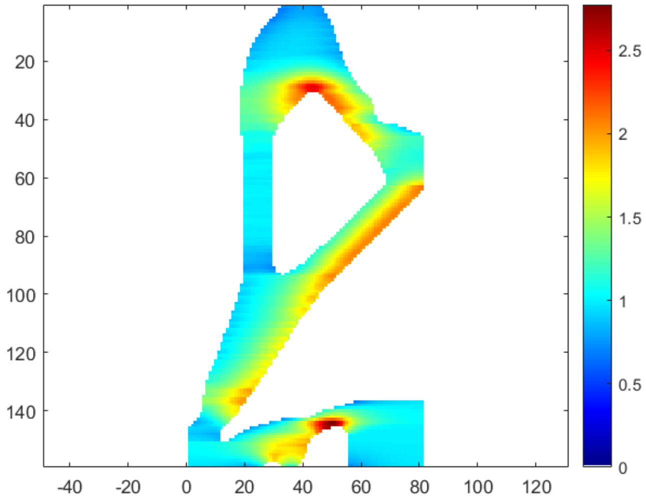

Figure B.8: Temperature field for the design obtained with robust CM TO with hotspot constraint, with a maximum relative temperature $T_{\text{crit}} = 2.77$

C

Extra TO with hotspot constraint results for various critical temperatures

This appendix consists of results from the robust topology optimization (TO) with hotspot constraint. The following results were obtained using a filter radius of 6, a volume fraction of 0.4 and a β multiplication factor of 1.2.

C.1. Critical temperature $T_{\text{crit}} = 2.42$

Figure C.1: Resulting eroded (left), intermediate (middle) and dilated (right) topologies from robust CM TO with hotspot constraint with an output displacement for the intermediate design $u_{\text{out}} = 35.1$.

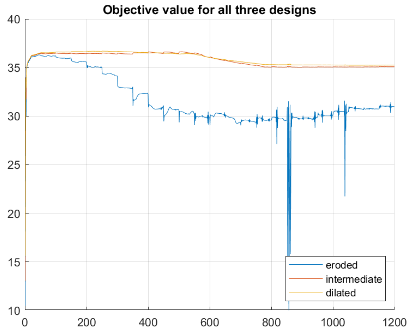

Figure C.2: Objective values of the eroded, intermediate and dilated designs per iteration

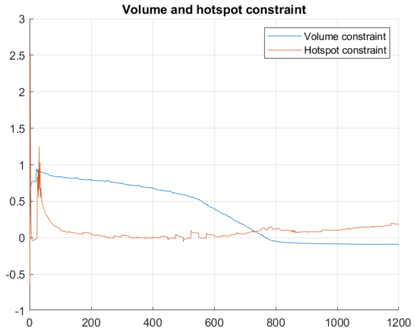

Figure C.3: Volume and hotspot constraint values per iteration

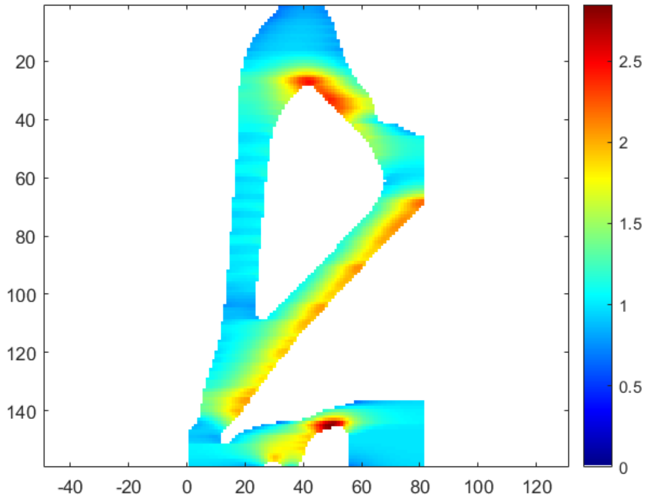

Figure C.4: Temperature field for the design obtained with robust CM TO with hotspot constraint, with a maximum relative temperature $T_{\text{crit}} = 2.85$

C.2. Critical temperature $T_{\text{crit}} = 4$

Figure C.5: Resulting eroded (left), intermediate (middle) and dilated (right) topologies from robust CM TO with hotspot constraint with an output displacement for the intermediate design $u_{\text{out}} = 35.4$.

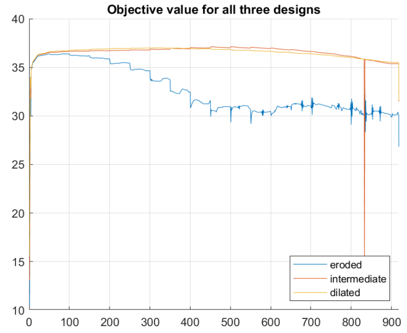

Figure C.6: Objective values of the eroded, intermediate and dilated designs per iteration

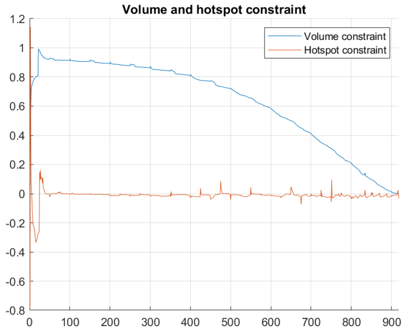

Figure C.7: Volume and hotspot constraint values per iteration

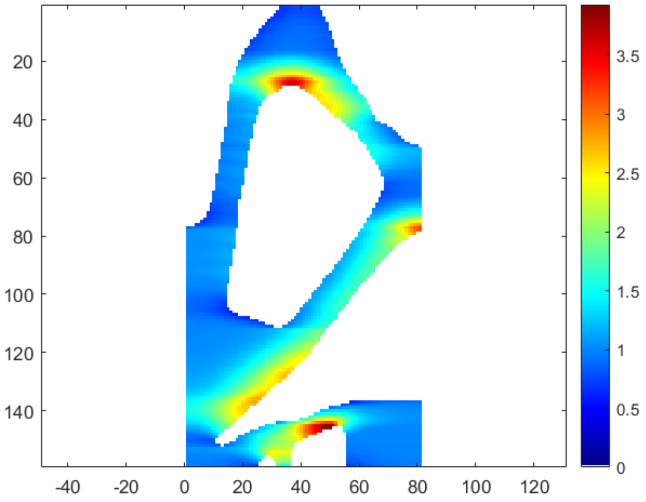

Figure C.8: Temperature field for the design obtained with robust CM TO with hotspot constraint, with a maximum relative temperature $T_{\text{crit}} = 3.93$